Quantification of load-dependent changes in the collagen fiber architecture for strut chordae tendineae-leaflet insertion of porcine atrioventricular heart valves

Colton J. Ross[1], Ming-Chen Hsu[2], Ryan Baumwart[3], Arshid Mir[4], Harold M. Burkhart[5], Gerhard A. Holzapfel[6,7], Yi Wu[1], and Chung-Hao Lee[1,8]

[1]Biomechanics and Biomaterial Design Laboratory (BBDL)
School of Aerospace and Mechanical Engineering
The University of Oklahoma
Norman, OK 73019, USA

[2]Department of Mechanical Engineering
Iowa State University
Ames, IA 50011, USA

[3]Department of Veterinary Clinical Sciences
College of Veterinary Medicine
Washington State University, Pullman, WA 99164, USA

[4]Department of Pediatric Cardiology
[5]Department of Surgery
The University of Oklahoma Health Sciences Center
Oklahoma City, OK 73104, USA

[6]Institute of Biomechanics
Graz University of Technology
Graz, Austria

[7]Department of Structural Engineering
Norwegian University of Science and Technology (NTNU)
Trondheim, Norway

[8]Institute for Biomedical Engineering, Science and Technology (IBEST)
The University of Oklahoma
Norman, OK 73019, USA

For correspondence:
Chung-Hao Lee, Ph.D.
Assistant Professor
School of Aerospace and Mechanical Engineering
Affiliated Faculty
Institute for Biomedical Engineering, Science and Technology
The University of Oklahoma
865 Asp Ave., Felgar Hall Rm. 219C
Norman OK 73019-3609, U.S.A.
email: ch.lee@ou.edu
Tel: +1-405-325-4842

1 **Abstract**

2   Atrioventricular heart valves (AHVs) regulate the unidirectional flow of blood through the heart by

3 opening and closing of the leaflets, which are supported in their functions by the chordae tendineae (CT).

4 The leaflets and CT are primarily composed of collagen fibers that act as the load-bearing component of

5 the tissue microstructures. At the CT-leaflet insertion, the collagen fiber architecture is complex, and has

6 been of increasing focus in the previous literature. However, these previous studies have not been able

7 to quantify the load-dependent changes in the tissue's collagen fiber orientations and alignments. In the

8 present study, we address this gap in knowledge by quantifying the changes in the collagen fiber

9 architecture of the mitral and tricuspid valve's strut CT-leaflet insertions in response to the applied loading

10 by using a unique approach, which combines polarized spatial frequency domain imaging with uniaxial

11 mechanical testing. Additionally, we characterized these microstructural changes across the *same*

12 *specimen* without the need for tissue fixatives. We observed increases in the collagen fiber alignments

13 in the CT-leaflet insertion with increased loading, as described through the degree of optical anisotropy.

14 Furthermore, we used a leaflet-CT-papillary muscle entity method during uniaxial testing to quantify the

15 chordae tendineae mechanics, including the derivation of the Ogden-type constitutive modeling

16 parameters. Results from this study provide a valuable insight into the load-dependent behaviors of the

17 strut CT-leaflet insertion, offering a research venue to better understand the relationship between tissue

18 mechanics and the microstructure, which will contribute to a deeper understanding of AHV biomechanics.

1. Introduction

The atrioventricular heart valves (AHVs) regulate the unidirectional flow of blood between the atria and the ventricles by cyclic opening and closing of the valve leaflets. Of the two AHVs, the mitral valve (MV) is composed of two leaflets, namely the MV anterior and posterior leaflets, whereas the tricuspid valve (TV) is comprised of three leaflets: the TV anterior, posterior, and septal leaflets (**Fig. 1a**). The AHV leaflets are assisted in their function by the chordae tendineae (CT), which attach to the papillary muscles to provide supporting forces during valve closure (Klabunde 2011). The CT can be classified based on their insertion location to the leaflet (Lam *et al.* 1970; Silver *et al.* 1971): (i) *basal* chordae attaching near the leaflet base, (ii) *marginal* chordae inserting near the free edge of the leaflet, and (iii) *strut* chordae, which are noticeably thicker, attaching to the central, belly region of the AHV anterior leaflet. The strut chordae tendineae are of particular interest in previous AHV biomechanics research as they are the primary load-bearing CT subset (Lam *et al.* 1970; Lomholt *et al.* 2002; Silver *et al.* 1971).

Failure or dysfunction of any sub-valvular component, such as in the case of chordae rupture, may lead to AHV regurgitation, in which there is a retrograde blood flow into the atrium during systole (Waller *et al.* 1994; Waller *et al.* 1995). Valve regurgitation is a prevalent issue, with MV and TV regurgitation affecting an estimated 7.8 million and 1.6 million people in the United States, respectively (Freed *et al.* 1999; Stuge and Liddicoat 2006). In severe cases, this pathology can worsen the quality of life through symptoms such as fatigue, exercise intolerance, or even lead to heart failure. There are many surgical treatments for AHV regurgitation; however, current therapeutics may suffer from issues of disease recurrence in the short- to long-term (Butany *et al.* 2004; Navia *et al.* 2010; Pfannmüller *et al.* 2012). In order to improve outcomes of these therapeutics, it is important to obtain a more comprehensive understanding of the proper function of the AHV structures, which will be used for developing predictive computer simulation tools that emulate natural valve mechanics and microstructures.

From the microstructural perspective, the AHV leaflets and chordae tendineae microstructures are primarily composed of collagen fibers (Liao *et al.* 2009; Lim and Boughner 1977). In their relaxed state, collagen fibers are crimped, and will uncrimp, elongate, and reorient in response to mechanical loading (Meador *et al.* 2020). Specific to the AHV leaflets, the collagen fibers reside within a layered

microstructure alongside elastin, glycosaminoglycans, and valvular interstitial cells (Kramer *et al.* 2019; Lee *et al.* 2015; Sacks *et al.* 2009). In the AHV leaflets, the collagen fiber architecture (CFA) is predominantly oriented to the leaflet tissue's circumferential direction, with additional fibers reorienting to the radial direction during cyclic cardiac loading (De Hart *et al.* 2004). On the other hand, the chordae tendineae also possess an intricate layered microstructure, organized from the outermost to the innermost: an endothelial cell layer, an elastin sheath with fibers oriented at inclined angles to the longitudinal axis, an elastin sheath with longitudinal fibers, a layer of circumferentially-aligned collagen fibers, and an inner core of straight collagen fibers and longitudinal elastin fibers (Millington-Sanders *et al.* 1998). The microstructures of both the leaflet and the chordae tendineae are connected through the CT-leaflet insertion, where the highly aligned collagen fibers of the chordae tendineae transition into the more complex CFA of the leaflet. Specifically, it has been found through histological analysis that the collagen fibers in the leaflet closer to the annulus are more preferentially aligned in the tissue's circumferential direction, and that the fibers become more aligned towards the radial direction approaching the CT-leaflet insertion (Chen *et al.* 2004). Another preliminary work used X-ray diffraction to investigate the CT-leaflet insertion microstructure, reporting higher molecular strains in the insertion than in the chordae segment or leaflet portions of the tissue, suggesting a higher rupture potential (Madhurapantula *et al.* 2020). To supplement these studies on the microstructure of the AHV leaflets, the chordae, and the CT-leaflet insertion, researchers have sought to characterize the mechanical properties of these sub-valvular components.

Many studies focused on the mechanical characterizations of the separated AHV leaflets (Clark 1973; Jett *et al.* 2018; Khoiy and Amini 2016; May-Newman and Yin 1995; Pokutta-Paskaleva *et al.* 2019), or the individual chordae tendineae segments (Gunning and Murphy 2015; Lim and Boughner 1975; Ritchie *et al.* 2006; Zuo *et al.* 2016). From these studies, it has been shown that both the leaflet and the CT tissues exhibit a distinct J-shape, nonlinear stress-strain behavior. More specifically, the AHV leaflets' radial directions were more extensible than the circumferential direction, and the tissues displayed unique mechanical properties between the two AHVs (i.e., MV vs. TV) and between leaflets within the same valves (e.g., MV anterior vs. posterior leaflet) (Jett *et al.* 2018). As for the chordae tendineae, it was found

75 that the strut CT were generally stiffer than the basal and marginal CT, and that the MV chordae were

76 generally stiffer than their TV counterparts (Pokutta-Paskaleva *et al.* 2019). While these foundational

77 studies have provided valuable information about the tissue biomechanics of the individual sub-valvular

78 components, very few consider the mechanics of the coupled CT-leaflet insertion.

79   Additionally, earlier works on the mechanics of the CT-leaflet insertion were conducted by using

80 mechanical testing devices or *in vitro* flow loops. For example, (Sedransk *et al.* 2002) performed uniaxial

81 tensile testing of the connected MV CT and leaflet and found the CT-leaflet insertion as the most rupture-

82 vulnerable area of the chordae. In another study, (Chen *et al.* 2004) used a unique biaxial testing system

83 where three edges of an MV anterior leaflet (MVAL) were attached via sutures, and the strut CT was

84 mounted as the fourth edge using string. From optical tracking-based surface strain quantification, they

85 found that approaching the CT-leaflet insertion, the radial extensibility of the tissue decreased while the

86 derived tangent modulus increased. In contrast to the use of mechanical testing devices, (Padala *et al.*

87 2010) studied the MVAL strut CT-leaflet insertion using an *in vitro* flow loop in conjunction with marker-

88 based optical tracking and found higher stretches in the edges of the insertion than in the center of the

89 insertion. Despite these research efforts, there is very limited information about connecting the load-

90 dependent changes in the CFA to the mechanics of the CT-leaflet insertion.

91   Thus, the overall objective of this study is to fill this gap in knowledge for the CT-leaflet insertion of

92 the AHVs by establishing the interrelationship between the quantified mechanical properties of leaflet-

93 CT-papillary muscle entities (**Fig. 1b**) and the changes in the underlying CFAs in response to the applied

94 loading. This is achieved by utilizing an integrated instrument (**Fig. 1c**) that facilitates uniaxial mechanical

95 testing and collagen fiber microstructural quantification based on polarized spatial frequency domain

96 imaging (pSFDI) (Goth *et al.* 2016). Through this pSFDI method, the load-dependent changes in the CFA,

97 including the collagen fiber orientation and the degree of optical anisotropy, of the CT-leaflet insertion are

98 quantified by using the *same specimen* without the use of chemical fixatives, offering an advantage

99 compared to the previous histological or *in vitro* flow loop study (Chen *et al.* 2004; Padala *et al.* 2010).

100 Findings of the present work will be useful for gaining a better understanding of the microstructure-

101 mechanics relationships in the atrioventricular heart valves, especially the CT-leaflet insertion, and

102 ultimately would lead to an improvement of treatments for heart valve disease, such as the synthetic

103 chordae replacements (Salvador *et al.* 2008; Seeburger *et al.* 2014).

104 **2. Methods**

105 2.1 Tissue preparation

106   Healthy porcine hearts (80-140 kg of weight, 1-1.5 years of age, 1:1 female-to-male ratio) were

107 obtained from a local USDA-approved abattoir (Chickasha Meat Co., Chickasha, OK, USA) within 12

108 hours of animal sacrifice. Hearts were transported to the laboratory, cleansed of blood clots, and stored

109 in a freezer at -20 °C until later testing. Freezing has been a common practice for effective tissue storage,

110 and prior studies have shown minimal changes in the tissue mechanics of heart valve leaflets and other

111 connective tissues following freezer storage (Duginski *et al.* 2020; Foutz *et al.* 1992; O'Leary *et al.* 2014;

112 Stemper *et al.* 2007; Venkatasubramanian *et al.* 2006).

113   At the time of tissue testing, hearts were thawed and dissected to remove the leaflet-CT-papillary

114 muscle entities from the MV and TV anterior leaflets (**Fig. 1a**) according to our previously-developed

115 procedure (Ross *et al.* 2020). In brief, the strut chordae tendineae were extracted such that the

116 attachments to the leaflet and papillary muscle (PM) were preserved, allowing for the specimen to be

117 considered as a whole entity (**Fig. 1b**). In this work, strut chordae tendineae were used, as opposed to

118 the basal or marginal chordae, because the strut CT are the most critical subset for carrying the

119 mechanical load *in vivo* (Lomholt *et al.* 2002). Once the leaflet-CT-PM entity specimens were prepared,

120 the chordae thickness was optically measured using a 12-megapixel camera under microscopy

121 (AmScope, Irvine, CA, USA) and analyzed in the ImageJ software (National Institute of Health, Bethesda,

122 MD, USA). Thickness measurements were taken at three locations along the central portion of the

123 unloaded (just mounted) strut CT segment, and an average of the three thickness measurements was

124 used for the subsequent tissue stress analysis (see **Section 2.3**).

125   By using tined-based BioRakes that pierced the leaflet and papillary muscles under a uniaxial testing

126 setup (**Fig. 1b**), the leaflet-CT-PM entity specimens were then mounted to a commercial biaxial

127 mechanical testing system equipped with 1.5N load cells – BioTester (CellScale Biomaterials Testing,

128 Waterloo, ON, Canada). This tine-based tissue mounting mechanism allowed for planar, uniaxial

129 deformation of the leaflet and papillary muscle attachments, emulating their respective *in vivo* mechanical

130 interactions. The leaflet-CT-PM entity specimens were then submerged in phosphate-buffered saline

131 (PBS) and heated to 32 °C. A temperature slightly lower than the body temperature (37 °C) was used to

132 avoid issues related to fogging of the polarizer lens during the pSDFI-based collagen microstructural

133 quantification procedure, as will be described in **Section 2.5**.

134 2.2 Uniaxial mechanical testing of the leaflet-CT-PM entity specimens

135   For uniaxial mechanical testing (**Fig. 1c**), MVAL and TVAL strut chordae entity specimens (n=12 for

136 each valve) were tested in the following three steps: preconditioning, pSFDI at various deformation

137 states, and mechanical testing. In the preconditioning step, leaflet-CT-PM entity specimens were

138 cyclically loaded and unloaded for ten times at a rate of 4.42 N/min to reach the targeted force, F_{max}, of

139 1.4 or 1.2N for the MVAL or TVAL strut chordae, respectively. The targeted force was selected based on

140 the physiologic loading experienced by the strut CT, as determined in a previous *in vitro* study (Jimenez

141 *et al.* 2003). The last unloading cycle was then considered for determining the six loading points from the

142 force-tine displacement curve (**Fig. 1d**) that were used in the subsequent pSFDI-based collagen

143 microstructural quantifications. Following the pSFDI procedure (see **Section 2.5**), fiducial markers were

144 positioned on the strut CT segment using a surgical pen, and five additional loading-unloading cycles

145 were performed that targeted the same F_{max} as the one used in the preconditioning step. For the

146 subsequent stress-stretch analysis, the final unloading cycle was used. Throughout testing, load cell force

147 readings and CCD camera-captured images were recorded at 5 Hz by the LabJoy program of the

148 CellScale BioTester.

149 2.3 Tissue stress and stretch calculations for the strut CT segments

150   Following the mechanical testing, tissue stress and stretch were quantified following the methods in

151 our previous work (Ross *et al.* 2020). In brief, the digital image correlation (DIC) module of the LabJoy

152 program was used to obtain the time-dependent coordinates of the centroid of the fiducial markers, i.e.,

153 (x_i, y_i) for the ith fiducial marker. Then, the fiducial marker's x- and y-displacements, (u_i, v_i), between

154 any two loading states were determined. The tissue stretch, λ_i, of the CT segment between marker i

155 and $i+1$ was calculated by using a 1D two-node linear finite element (Hughes 1987)

$$\lambda_i = 1 + \frac{1}{L_i}\left(d_{i+1} - d_i\right),\tag{1}$$

157 where $L_i = \sqrt{(x_{i+1} - x_i)^2 + (y_{i+1} - y_i)^2}$ is the distance between the two adjacent markers, and d_i are the

158 displacements of these markers along the direction parallel to the CT segment's direction, i.e.,

159 $d_i = u_i \cos\theta + v_i \sin\theta,$ $d_{i+1} = u_{i+1}\cos\theta + v_{i+1}\sin\theta,$ and $\tan\theta = (y_{i+1} - y_i)/(x_{i+1} - x_i),$ and θ is the angle

160 between the markers. Then, the tissue stretch of the CT segment was obtained by averaging the stretch

161 values of those finite elements associated with the fiducial markers, i.e., $\lambda = \frac{1}{m}\sum_{i=1}^{m}\lambda_i$, where m is the

162 number of 1D linear finite elements. The tissue's Cauchy stresses were determined by

$$\sigma = \left(\frac{F}{A_0}\right)\lambda,\tag{2}$$

164 where F is the applied force, and A_0 is the undeformed cross-sectional area. All the mechanical values

165 (i.e., stress, stretch) were determined at the peak load $F_{\max}$, with respect to the post-preconditioning

166 configuration. Chordae were idealized as a circular cross-sectional area, $\pi D^2/4$, where D is the measured

167 (undeformed) thickness of the CT (see **Section 2.1**).

168 2.4 Constitutive modeling of tissue mechanics for strut CT segments

169   To supplement the information on the tissue mechanics for the strut CT, constitutive modeling was

170 performed, in which the CT were considered as nonlinear, isotropic, incompressible solids, modeled by

171 the one-term Ogden hyperelastic model (p=1) (Ogden 1972)

$$\sigma = \mu\left(\lambda^{\alpha} - \lambda^{-\alpha/2}\right),\tag{1}$$

173 where σ is the Cauchy stress, λ is the tissue stretch as determined from **Section 2.3**, and μ and α are

174 the two Ogden model parameters. The parameters μ and α represent the stress transition between the

175 low- and high-tension regimes and the post-transition stiffness, respectively.

176   The two model parameters were determined by nonlinear least-squares fitting to the tissue stress-

177   stretch data by using an in-house differential evolution optimization program (**Fig. 2**), considering a

178   residual error tolerance of 10^{-10} (Storn and Price 1997). To examine the goodness of fit, the normalized

179   root-mean-square-deviation (NRMSD) was used, which is the square root of the average of the squared

180   errors, normalized with respect to the maximum Cauchy stress value.

181   2.5 pSFDI-based collagen fiber microstructural quantification

182   Following the procedure our lab developed for characterizing bovine tendon and representative

183   MVALs (Jett *et al.* 2020), the pSFDI system (**Fig. 1c**) operates as follows: (i) the light shines from a

184   projector, (ii) the light passes through a polarizer at an angle $\theta_{\mathrm{polarizer}}$ and onto the sample, (iii) the

185   polarized light reflects from the sample's collagen fibers back through the same polarizer, and (iv) the

186   intensity of the reflected light is captured by a camera. Steps (i-iv) are repeated with $\theta_{\mathrm{polarizer}}$ ranging from

187   0° to 180° with a 5° increment.

188   The above-mentioned loading points of the force-displacement curve (**Fig. 1d**) were determined from

189   an intermediate study, in which 9 different deformation states between the unloaded (relaxed) state Ω_0

190   and the peak loading F_{max} were considered. The above pSFDI procedure was performed at each of these

191   deformation states, in which the MVAL or TVAL strut chordae entity was stretched at the corresponding

192   tine displacement. Then, the CFA was analyzed from the acquired pSFDI data (see more details in

193   **Section 2.6**), and the changes in the predicted collagen fiber angle θ_{fiber} and degree of optical anisotropy

194   were quantified. The loading points were selected based on those with the most noticeable changes,

195   while keeping the total test duration to a reasonable timeframe (<2 hours per specimen). From our internal

196   study, the loading points were determined as (**Fig. 1d**):

197   • *Loading Point 0* – tissue mounting configuration Ω_0 (zero force, zero deformation)

198   • *Loading Point 1* – intermediate point between Ω_0 and the post-preconditioning configuration Ω_1

199   • *Loading Point 2* – post-preconditioning configuration Ω_1

200   • *Loading Point 3* – intermediate point between Ω_1 and $0.3F_{\mathrm{max}}$

201   • *Loading Point 4* – 30% of the peak force $0.3F_{\mathrm{max}}$

202   • *Loading Point 5* – peak force F_{max}.

203   After the preconditioning cycle, the integrated pSFDI-biaxial testing system (**Fig. 1c**) was used for

204 capturing the birefringent light intensity responses of the CFA of the MVAL and TVAL leaflet-CT-PM entity

205 specimens. The pSFDI procedure, as described previously, was repeated at each of the six loading

206 points, and the acquired images (1280x1024 pixels) were further analyzed. The images were then

207 processed to determine the pixel-wise fiber orientation angle θ_{fiber} and the degree of optical anisotropy

208 (DOA), a metric that is related to the alignment of the collagen fiber networks of the tissue (i.e., smaller

209 values of DOA denote a random fiber network, whereas larger values of DOA signify highly-aligned

210 fibers). The pSFDI image data analysis is described in **Section 2.6**. After the pSFDI procedure, the CT

211 entity specimens were uniaxially tested using the procedure described in **Section 2.2**.

212 2.6 Analysis of pSFDI-based collagen microstructural data

213   Tissue collagen fiber orientations were determined following the methods described in our previous

214 work (Jett *et al.* 2020), and the theory outlined in (Goth *et al.* 2016). In pSFDI, as $\theta_{\text{polarizer}}$ is rotated from

215 0° to 180° the intensity of the reflected polarized light *I* returns a bimodal response due to the birefringent

216 response of the collagen fibers (**Fig. 3**). The bimodal response contains a global maximum when $\theta_{\text{polarizer}}$

217 is equal to θ_{fiber}, and a local maximum when $\theta_{\text{polarizer}}$ is 90° offset from θ_{fiber}. The bimodal intensity

218 response *I* can then be described using the 3-term Fourier series:

$$I = \gamma_0 + \gamma_2 \left[2\left(\theta_{fiber} - \theta_{polarizer} \right) \right] + \gamma_4 \left[4\left(\theta_{fiber} - \theta_{polarizer} \right) \right], \tag{2}$$

220 where the Fourier constants are γ_0, which represents the mean light intensity, and γ_2 and γ_4, which

221 describe the optical anisotropy. The degree of optical anisotropy (DOA) can then be computed by

$$DOA = \frac{\gamma_2 + \gamma_4}{\gamma_0 + \gamma_2 + \gamma_4}. \tag{3}$$

223 In this work, we focused on predicting the average collagen fiber angles and DOA through the full

224 thickness of the strut CT-leaflet insertion. Thus, the spatial frequency domain imaging theory and the

225 corresponding variable tissue-depth imaging are not described. We refer the reader to some previous

226 works (Cuccia *et al.* 2005; Goth *et al.* 2019; Jett *et al.* 2020; Mazhar *et al.* 2014).

227   For the investigations of the load-dependent changes in the CFA of the MVAL/TVAL strut chordae

228 entities, two regions of interest (ROIs) were defined (**Fig. 1b** and **Fig. 3b**): (i) the CT segment (n=7 for

229 MVAL; n=7 for TVAL) and (ii) the CT-leaflet insertion (n=10 for MVAL; n=8 for TVAL). Variations in the

230 number of available specimens in the pSFDI data analysis were due to the limited field of view within the

231 polarizer lens window. Within the analyzed ROIs, the average θ_{fiber}, the average DOA, and the percent

232 differences in the DOA were quantified to evaluate changes in the CFA in response to mechanical loads.

233   To further examine the spatial variations in the CFA, the CT-leaflet insertion was subdivided into 9

234 sub-regions using a uniform 3x3 grid (**Fig. 1e**). To elaborate, the ROI of the CT-leaflet insertion was

235 transformed to a parametric space (similar to the isoparametric mapping concept in the finite element

236 methods, see (Hughes 1987)), and the 3x3 grid array was generated to ensure uniformity in the physical

237 domain (**Fig. 4**). Within each sub-region, the average θ_{fiber}, the average DOA, and the percent changes

238 in the DOA were analyzed and reported.

239 2.7 Statistical analysis

240   To determine statistically-significant changes in θ_{fiber} and the DOA between the six loading points for

241 the MVAL or TVAL chordae entities, one-way analysis of variance (ANOVA) was performed using an in-

242 house MATLAB program (MathWorks, Natick, MA). For ANOVA, comparisons were only made between

243 specimens within their respective groups: the MVAL or the TVAL chordae entities. To verify the use of

244 one-way ANOVA, quantile-quantile (QQ) plots were generated to confirm the general normality of the

245 data (**Figs. S1-S8** in the **Supplementary Material** section). If a p-value <0.05 was found in the one-way

246 ANOVA, a multiple comparison was next performed by using the `multcompare` function of MATLAB

247 to determine significant differences pairwise between each loading point. In this study, we considered p-

248 values <0.05 as statistically significant, indicating that the quantified DOA or the predicted fiber orientation

249 angle was significantly different between the compared loading points.

250 **3. Results**

251 3.1 Thickness measurement, mechanical testing and constitutive modeling results

252   The tissue thicknesses were found as 0.86±0.07 mm and 1.19±0.08 mm for the TVAL and the MVAL

253   strut CT, respectively (**Fig. 5a**). Using the tissue thicknesses and the recorded load cell force readings

254   from uniaxial testing, the Cauchy stresses were computed and reported as follows: 2.54±0.32 MPa for

255   the TVAL strut CT entities and 1.49±0.21 MPa for the MVAL strut CT entities (**Fig. 5b**). In addition, the

256   stretches for the TVAL and MVAL strut CT entities were 1.027±0.004 and 1.028±0.005, respectively (**Fig.**

257   **5c**). The Cauchy stress-stretch data was used to estimate the Ogden model parameters via nonlinear

258   least-squares regression (**Fig. 5d-e**), and reported as follows: parameter μ =176.54±42.11 kPa and

259   parameter α =128.53±13.43 for the TVAL strut CT, and μ =26.10±7.95 kPa and α = 210.94±19.02 for

260   the MVAL strut CT. For all the parameter estimations, the NRMSD was less than 0.1, suggesting a good

261   fit in our parameter estimations.

262   3.2 Collagen fibers architecture quantification results

263   Representative pSFDI-quantified load-dependent CFA results from an individual TVAL and MVAL

264   strut CT entity are shown in **Figures 6-7**, respectively. We noticed that the collagen fibers in both the CT-

265   leaflet insertion and the CT segment were predominantly oriented towards the loading direction (i.e., θ_{fiber}

266   =90°). Interestingly, the average θ_{fiber} for the strut CT entity had a minimal change in response to the

267   applied uniaxial loading (i.e., changes between tissue mounting and peak loading: <4% for the

268   representative TVAL and <1% for the representative MVAL). In contrast, noticeable changes were found

269   in the quantified DOA with increased loading (i.e., up to 29% and 45% changes for the representative

270   TVAL and MVAL CT segments, respectively, between tissue mounting and peak loading). Furthermore,

271   for both representative specimens, we saw the largest increase in the DOA between Loading Point 4

272   ($0.3F_{max}$) and Loading Point 5 (F_{max}).

273   In the following subsections the load-dependent CFA results, as quantified by pSFDI, are presented

274   for the *CT segment*, the *CT-leaflet insertion*, and the *sub-regions of the CT-leaflet insertion*, respectively.

275   In these results, we focused on comparing the changes in the quantified θ_{fiber} and DOA between any two

276   sequential loading points, or between two selected non-sequential loading points, i.e., between Loading

277 Point 0 and Loading Point 5 (i.e., tissue mounting vs. peak loading), and between Loading Point 2 and

278 Loading Point 5 (i.e., post-preconditioning vs. peak loading).

279 *3.2.1 Load-dependent changes in the CFA for the CT segment*

280 For the CT segments (see the schematic definition in **Fig. 1b**), we did not notice significant changes

281 in θ_{fiber} with increased loading (TVAL, p=0.975; MVAL, p=0.998, **Table 1**). In general, across all the six

282 loading points, the predicted θ_{fiber} was ~66° for the TVAL CT segments, and ~73° for the MVAL CT

283 segments. On the other hand, we did observe notable changes in the quantified DOA in response to the

284 applied loads, with several key findings summarized as follows. First, we found that the DOAs in the

285 TVAL CT segments are generally larger than those in the MVAL CT segments, suggesting a better

286 alignment of collagen fibers in the TVAL CT than their MVAL counterparts (TVAL, DOA=0.14-0.20; MVAL,

287 DOA=0.09-0.15, **Table 1**). Note that statistical comparisons were not made between the TVAL and the

288 MVAL, because the target peak loads were different for the specimens from the two AHVs. Second, when

289 considering changes in the DOA between the sequential loading points, the TVAL CT segments had

290 larger increases between Loading Point 4 and Loading Point 5 (20.4±2.6%) than between the other

291 sequential loading points (-0.5-7.1%) (**Table 2**). In contrast, for the MVAL CT segments, the increases in

292 the DOA between the sequential loading points were very similar, i.e., 13.9±3.5% changes between

293 Loading Point 2 and Loading Point 3, 13.3±9.5% changes between Loading Points 3 and 4, and

294 11.4±5.5% changes between Loading Point 4 and Loading Point 5. Thirdly, when comparing the changes

295 in the DOA between the non-sequential loading points, there were statistically-significant changes found

296 in the TVAL CT segments both between Loading Point 0 and Loading Point 5 (35.6±7.0%, p<0.001), and

297 between Loading Point 2 and Loading Point 5 (25.3±4.2%, p=0.001). For the MVAL CT, a statistically-

298 significant change in the DOA was only found between Loading Point 0 and Loading Point 5 (46.4±8.7%,

299 p=0.036), but not between Loading Point 2 and Loading Point 5 (38.3±7.5%, p=0.126).

300 *3.2.2 Load-dependent changes in the CFA for the CT-leaflet insertion*

301 For the strut CT-leaflet insertion (see the schematic definition in **Fig. 1b**), the predicted θ_{fiber} did not

302 vary significantly with the applied loading (TVAL, p=0.615; MVAL, p=0.990). Across all the six loading

303 states, θ_{fiber} was found to be ~72° and ~78° for the TVAL and MVAL CT-leaflet insertions, respectively

304 (**Table 3**). In contrast, there were some noticeable increases in the quantified DOAs with increased

305 applied loads (**Table 3**). For example, considering the sequential loading points, we observed the largest

306 increase in the DOA for the CT-leaflet insertions between Loading Point 4 and Loading Point 5 (TVAL:

307 18.3±2.6%, p=0.202; MVAL: 15.6±2.4%, p=0.039) (**Table 4**). For the TVAL CT-leaflet insertions, the

308 second largest increase in the DOA was from Loading Points 0 to 1 (7.4±1.2%, p=0.980), whereas it was

309 from Loading Points 2 to 3 for the MVAL CT-leaflet insertions (9.9±2.5%, p=0.567).

310 Considering the non-sequential loading points, there were statistically-significant differences in the

311 DOA for the TVAL CT-leaflet insertions between Loading Point 0 and Loading Point 5 (i.e., tissue

312 mounting vs. peak loading, 37.7±4.0%, p=0.002), and between Loading Points 2 and 5 (i.e., post-

313 preconditioning vs. peak loading, 25.3±3.7%, p=0.032). Similarly, for the MVAL CT-leaflet insertions,

314 statistically-significant differences in the DOA were found between Loading Point 0 and Loading Point 5

315 (37.5±2.8%, p<0.001), and between Loading Point 2 and Loading 5 (30.2±2.4%, p<0.001).

316 *3.2.3 Load-dependent changes in the predicted fiber orientation angle for the sub-regions in the CT-*

317 *leaflet insertion*

318 From the sub-regional analysis of the load-dependent CFA results of the TVAL and MVAL CT-leaflet

319 insertions (**Fig. 1e**), we observed that collagen fibers were more aligned toward the primary loading

320 direction (i.e., 90°) on the left edge (sub-regions 1, 4, and 7) than in the center (sub-regions 2, 5, and 8)

321 and on the right edge (sub-regions 3, 6, and 9) (**Tables 6-7**). Interestingly, although we did not notice

322 discernible changes in the predicted θ_{fiber} when the CT-leaflet insertion was analyzed as one whole entity

323 in **Section 3.2.2**, there were some statistically-significant changes in the predicted θ_{fiber} after dividing the

324 CT-leaflet insertion into the sub-regions. For example, when we analyzed the sequential loading points,

325 statistically-significant changes in θ_{fiber} were found between Loading Point 4 and Loading Point 5: sub-

326 region 8 of the TVAL CT-leaflet insertion (-1.19±0.95%, p=0.037), and sub-region 5 (0.71±1.16%,

327 p=0.018) and sub-region 8 (-4.61±1.69%, p=0.002) of the MVAL CT-leaflet insertion.

328   Considering the non-sequential loading points, statistically-significant differences in θ_{fiber} were found

329   in several sub-regions of the TVAL CT-leaflet insertion between Loading Point 0 and Loading Point 5

330   (i.e., tissue mounting vs. peak loading, sub-region 1: -6.35±1.85%, p=0.015, sub-region 2: -5.99±1.48%,

331   p=0.005, sub-region 4: -6.60±1.98%, p=0.008, sub-region 5: -6.73±2.26%, p=0.008, and sub-region 8:

332   -5.70±1.95%, p<0.001), as well as between Loading Point 2 and Loading Point 5 (i.e., post-

333   preconditioning vs. peak loading, sub-region 8: -2.69±1.63%, p<0.001). On the other hand, in the MVAL

334   CT-leaflet insertions, statistically-significant differences in θ_{fiber} were found between Loading Point 0 and

335   Loading Point 5 (sub-region 1: 1.38±2.78%, p=0.025, sub-region 2: 1.11±1.42%, p<0.001, sub-region 3:

336   -2.51±3.46%, p<0.001, sub-region 5: -0.59±1.62%, p<0.001, sub-region 6: 1.17±2.09%, p=0.008, and

337   sub-region 8: -7.79±1.98%, p<0.001), and between Loading Point 2 and Loading Point 5 (sub-region 2:

338   0.21±1.13%, p<0.001, sub-region 3: 0.55±2.54%, p<0.001, sub-region 5: -0.32±1.27%, p<0.001, sub-

339   region 6: -0.14±1.87%, p=0.023, and sub-region 8: -5.90±1.95%, p<0.001).

340   *3.2.4 Load-dependent changes in the quantified DOA for the sub-regions in the CT-leaflet insertion*

341   Considering the load-dependent changes in the quantified DOAs between the sequential loading

342   points, we observed the largest change from Loading Points 4 to 5, and the smallest from Loading Points

343   3 to 4 (**Fig. 8** and **Tables 5-6**). Specifically, we found a statistically-significant increases in the DOA

344   between Loading Point 4 and Loading Point 5 for sub-region 8 (20.63±3.87%, p=0.037) of the TVAL CT-

345   leaflet insertions, as well as sub-region 5 (18.19±3.05%, p=0.018) and sub-region 8 (20.47±4.26%,

346   p=0.017) of the MVAL CT-leaflet insertions. We generally found an increase in the DOA with increased

347   loading; however, we did notice decreases in the DOA between some sequential loading points, i.e.,

348   between Loading Point 0 to Loading Point 1: sub-region 4 (-1.76±2.65%, p=0.999) and sub-region 6

349   (-1.39±4.31%, p=0.999) of the MVAL CT-leaflet insertions; between Loading Point 3 to Loading Point 4:

350   sub-region 3 (-17.32±7.90%, p>0.05) of the TVAL CT-leaflet insertions, and sub-region 1 (0.05±7.92%,

351   p=0.999) and sub-region 6 (6.00±3.24%, p=0.994) of the MVAL CT-leaflet insertions.

352   Additionally, changes in the quantified DOA between the non-sequential loading states were also

353   found between Loading Point 0 and Loading Point 5 (i.e., tissue mounting vs. peak loading), and between

354 Loading Point 2 and Loading Point 5, i.e., post-preconditioning vs. peak loading (**Table 7**). Specifically,

355 for the TVAL CT-leaflet insertions, the largest increase in the DOA was found to be sub-region 1

356 (46.3±6.2%, p=0.015) between Loading Point 0 and Loading Point 5, and sub-region 2 (50.1±4.8%,

357 p=0.053) between Loading Point 2 and Loading Point 5. In contrast, for the MVAL CT-leaflet insertions,

358 the largest increase in the DOA was observed in sub-region 2 from Loading Points 0 to 5 (37.3±2.6%,

359 p<0.001) and from Loading Points 2 to 5 (30.0±3.1%, p<0.001). Moreover, statistically-significant

360 increases in the quantified DOA for the non-sequential loading were found between Loading Point 0 to

361 Loading Point 5: sub-regions 1, 2, 4, 5, 8, and 9 of the TVAL CT-leaflet insertions (0.001<p<0.016), and

362 sub-regions 1, 2, 3, 5, 6, and 8 of the MVAL CT-leaflet insertions (0.001<p<0.025), as well as between

363 Loading Points 2 and Loading Point 5: sub-region 8 of the TVAL CT-leaflet insertions (p<0.001), and sub-

364 regions 2, 3, 5, 6, and 8 of the MVAL CT-leaflet insertions (0.001<p<0.023).

365 **4. Discussion**

366 4.1 General findings and comparisons with existing literature

367   We found that the stretches of the MVAL and TVAL strut CT were similar under their respective

368 targeted tension (**Fig. 5**). Comparing to previous studies on characterizing the mechanics of chordae

369 tendineae, lower stretches were observed in our study than those reported in the previous testing of

370 individual strut chordae segments (Liao and Vesely 2003; Lim 1980; Lim and Boughner 1975; Lim and

371 Boughner 1976; Pokutta-Paskaleva *et al.* 2019; Ritchie *et al.* 2006; Zuo *et al.* 2016), but the stretches

372 were similar to our previous study on the leaflet-CT-PM entities (Ross *et al.* 2020). In addition, the Ogden

373 constitutive model parameters were determined from nonlinear least-squares fitting to uniaxial

374 mechanical data, and the parameter μ was generally larger for the TVAL strut CT than their MVAL

375 counterparts, while the parameter α was larger for the MVAL strut CT. This suggests that the MVAL

376 strut CT have a lower stress-transition in the low- and high-tension regimes, and that the TVAL strut CT

377 have a higher post-transition stiffness. Additionally, the constitutive model parameters determined in the

378 present study were similar to those reported in our previous study (Ross *et al.* 2020), and within a similar

379 range from other mechanical testing studies on individual strut CT segments (Pokutta-Paskaleva *et al.*

380 2019; Zuo *et al.* 2016).

381   From the pSFDI-based collagen microstructural quantifications, we examined the load-dependent

382 changes in the CFAs of both the CT segments and the CT-leaflet insertions. Specifically, collagen fibers

383 of both the CT segments and the CT-leaflet insertions were mostly oriented towards the primary loading

384 direction of 90° (**Figs. 6-7**), with indiscernible changes in the collagen fiber orientations with increased

385 loading (**Tables 1**, **3**). The minimal changes in θ_{fiber} and the slight deviation of the collagen fibers in the

386 CT segments from the 90° direction may be explained by collagen fiber crimping and uncrimping or by

387 planar waves of collagen fibers as previously described by (Millington-Sanders *et al.* 1998). Interestingly,

388 we did notice changes in θ_{fiber} when the CT-leaflet insertion was divided into nine sub-regions; however,

389 there was no clear and consistent trend in the collagen fiber reorientations within the CT-leaflet insertions.

390   In addition, we observed increases in the quantified DOA with the applied loading, indicating a better

391 alignment of the collagen fibers from the unloaded to the loaded states (**Tables 1-4**). Generally, the

392 greatest increase in the quantified DOA was from Loading Points 4 and 5 (i.e., $0.3F_{\text{max}}$ vs. F_{max}) for both

393 the CT segments and the CT-leaflet insertions, suggesting more rapid alignments of the collagen fibers

394 in the high-tension than in the low-tension regime. Comparing the tissue mounting and post-

395 preconditioning configurations to the peak loading, the DOA increased up to 50%. Those increases in

396 the DOA without major collagen fiber reorientations may be explained by the uncrimping of collagen fibers

397 in response to the increased loads. This findings agree with the observations in our previous study on

398 testing the central, belly region of the MVAL tissue under equibiaxial loading (Jett *et al.* 2020). In that

399 study, the collagen fiber orientations of the tissue mostly remained the same between the unloaded and

400 loaded states, whereas clear increases in the DOA were found.

401   Furthermore, previous literature is limited when comparing to our collagen microstructural

402 quantification results. In particular, no study has yet quantified the load-dependent behaviors of the

403 collagen fibers in the strut CT-leaflet insertion for the AHVs. (Padala *et al.* 2010) investigated the

404 mechanical behaviors of the MVAL strut CT-leaflet insertion by using an *in vitro* flow loop together with

405 optical marker tracking of the CT-leaflet insertion to obtain surface strains. They found that the edges of

406 the CT-leaflet insertion stretched more than the central portions. To complement their findings of the

407 regional variations in the tissue extensibility, we observed some greater increases in DOA in central

408 portions of the CT-leaflet insertion, as well as the increases in some of the edge regions (**Fig. 8** and

409 **Table 7**). (Padala *et al.* 2010) also analyzed the CT-leaflet insertion using small angle light scattering and

410 noted a higher alignment of collagen fibers in the CT segment, and that the collagen fibers transitioned

411 into a more disorganized network in the leaflet insertion. In another previous study using light microscopy,

412 (Chen *et al.* 2004) found similar orientations of collagen fibers in the MVAL strut CT-leaflet insertion to

413 those reported by (Padala *et al.* 2010); however, (Chen *et al.* 2004) also noticed the circumferentially-

414 oriented collagen fibers in the leaflet tissue closer to the annulus. In our study, we noticed some higher

415 DOA values in the CT segments than the CT-leaflet insertions, but the differences in the predicted θ_{fiber}

416 were not noticeable (**Figs. 6-7** and **Tables 1**, **3**). The difference in the findings between our present study

417 and the two previous studies may be attributed to the amount of leaflet tissue preserved beyond the CT-

418 leaflet insertion, i.e., from the belly region of the leaflet up to the annulus.

419   Findings from our study also provide insight into the differences between the mitral and the tricuspid

420 valves. For example, with the CFAs, we noticed generally greater increases in the DOA for the MV

421 chordae-leaflet insertion than for the TV. For tissue mechanics, we observed a lower stress-transition

422 stiffness in the MV specimens, whereas the TV specimens had a greater post-transition stiffness. These

423 findings could be related to the diverging natural designs of the two atrioventricular valves, such as the

424 differences in the number of leaflets, the structure and number of chordae, and the thicknesses of the

425 tissues due to their respective distinct physiological function and mechanical environment. It is important

426 to note that we tested the MV and TV chordae-leaflet insertion specimens at different force magnitudes

427 (MV, 1.4N; TV, 1.2N). Hence comparisons of the results between the two AHVs must be made with

428 caution.

429 4.2 Study limitations and future extensions

430   There are a few limitations existent in this study. First, the integrated pSFDI-biaxial testing system

431 had a limited field of view of the camera that did not allow for imaging of the entire CT-leaflet insertion for

432 some tissues specimens, resulting in a slightly-reduced sample size for the CT segments or the CT-

433 leaflet insertions. Second, there were some small mispredictions in the collagen fiber orientations

434 (**Figs. 6-7**), which may be due to the birefringent response of the collagen fibers, or tissue surface

435 imperfections such as tissue folding. In our work, tissues were mounted to the system with care to ensure

436 that minimal surface imperfections were present to limit the potential for mispredictions of θ_{fiber}. Third,

437 the physical interpretation of the quantified DOA is not yet fully established as to how it is related to the

438 degree of collagen fiber alignment. The DOA is a function of the optical anisotropy, as opposed to

439 structural anisotropy-based metrics such as the normalized orientation index (NOI) described in previous

440 works (Goth *et al.* 2019; Sacks *et al.* 1997). Fourth, in our tissue mounting procedure, we ensured the

441 tine-to-insertion distance was consistent as of ~3-5mm; however, the boundary condition may influence

442 the quantified load-dependent changes in the CFA, which warrants another future examination.

443   Future extensions of the present work include the analysis of the leaflet deformations, increasing the

444 polarizer field of view, assessing the CT failure mechanics, and testing other CT subsets (i.e., the

445 marginal and basal CT). To elaborate, in our study we did not provide a detailed strain mapping for the

446 leaflet-insertion, such as performed with the optical marker approach used by (Padala *et al.* 2010), and

447 thus, it would be a useful extension to further enhance our findings. In addition, the pSFDI-modality could

448 be useful in connecting the CT failure mechanics to the underlying microstructural changes, especially if

449 tissues were tested until failure using a modified pSFDI approach with a near real-time or real-time

450 imaging capability (Konecky *et al.* 2011). Use of the leaflet-CT-PM entity method performed in this work

451 would be a good supplement to the solely mechanics-based findings from the previous investigation of

452 CT failure (Sedransk *et al.* 2002). Another useful future extension could include analyses of the CT-leaflet

453 insertion using the spatial frequency domain imaging capabilities of our pSFDI system to understand the

454 load-dependent changes in the CFA at different light penetration depths of the tissue. Finally, the

455 methodology presented herein could be useful to analyze human tissues (healthy vs. diseased) to further

456 elucidate the subtle changes in valve biomechanics associated with valvular heart diseases.

457 4.3 Conclusion

458   In this study, *for the first time*, we have quantified the load-dependent changes in the collagen fiber

459   architecture of the strut CT-leaflet insertions of the AHV anterior leaflets by using the integrated pSFDI-

460   uniaxial testing and the leaflet-CT-PM entity approach. The pSFDI-based collagen microstructural

461   quantifications in our study for both the CT segments and the CT-leaflet insertions could serve useful for

462   understanding the recruitment of collagen fibers by emulating physiological loading conditions. Moreover,

463   we have also provided information on the stress-stretch behaviors of the CT segments through the tine-

464   based, cyclic uniaxial testing, which allowed for predictions of the Ogden-type constitutive model

465   parameters. Results from this study will be beneficial in developing a better understanding of the tissue

466   mechanics-microstructure relationships of the AHVs – a field of increasing interest in the biomechanics

467   community, such as in growth and remodeling frameworks (Cyron and Humphrey 2017; Horvat *et al.*

468   2019). Furthermore, the information from this study could be useful as a first look into better

469   understanding of chordae rupture, based on the quantified DOA of the CT-leaflet insertions, or for

470   incorporating the collagen fiber kinematics into the AHV computational models. To elaborate, the

471   information obtained from this study could be useful in AHV simulations with full 3D models of the chordae

472   (Toma *et al.* 2016), in which the transition region between the chordae and the leaflet can be better

473   defined. In addition, a better insight could be provided into how the chordae and the insertion areas

474   influence the healthy valve behaviors, or in cases of valvular disease and subsequent surgical repairs.

475   Changes in the chordae-insertion, chordae, or leaflet mechanics, such as in the case of a stenotic heart

476   valve or chordae rupture, could lead to leaflet prolapse scenarios and subsequent heart valve

477   regurgitation, and thus, better knowledge of the heart valve structures is critical to better understand the

478   underlying mechanisms of failure, and the best methods for repair to minimize disease recurrences.

Acknowledgments

Conflicts of Interest

The authors of this paper have no financial or personal relationships with other people or organizations that could inappropriately influence (bias) our work.

References

Butany J, Collins MJ, David TE (2004) Ruptured synthetic expanded polytetrafluoroethylene chordae tendinae. Cardiovascular Pathology 13:182-184. doi:10.1016/S1054-8807(04)00006-7

Chen L, Yin FC, May-Newman K (2004) The structure and mechanical properties of the mitral valve leaflet-strut chordae transition zone. Journal of Biomechanical Engineering 126:244-251. doi:10.1115/1.1695569

Clark RE (1973) Stress-strain characteristics of fresh and frozen human aortic and mitral leaflets and chordae tendineae. Implications for clinical use. Journal of Thoracic and Cardiovascular Surgery 66:202-208. doi:10.1016/S0022-5223(19)40619-3

Cuccia DJ, Bevilacqua F, Durkin AJ, Tromberg BJ (2005) Modulated imaging: Quantitative analysis and tomography of turbid media in the spatial-frequency domain. Optics Letters 30:1354-1356. doi:10.1364/ol.30.001354

Cyron CJ, Humphrey JD (2017) Growth and remodeling of load-bearing biological soft tissues. Meccanica 52:645-664. doi:10.1007/s11012-016-0472-5

De Hart J, Peters GWM, Schreurs PJG, Baaijens FPT (2004) Collagen fibers reduce stresses and stabilize motion of aortic valve leaflets during systole. Journal of Biomechanics 37:303-311. doi:10.1016/s0021-9290(03)00293-8

Duginski GA, Ross CJ, Laurence DW, Johns CH, Lee C-H (2020) An investigation of the effect of freezing storage on the biaxial mechanical properties of excised porcine tricuspid valve anterior leaflets. Journal of the Mechanical Behavior of Biomedical Materials 101:103438. doi:10.1016/j.jmbbm.2019.103438

Foutz TL, Stone EA, Abrams CF, III (1992) Effects of freezing on mechanical properties of rat skin. American Journal of Veterinary Research 53:788-792

Freed LA et al. (1999) Prevalence and clinical outcome of mitral-valve prolapse. New England Journal of Medicine 341:1-7. doi:10.1056/NEJM199907013410101

Goth W, Potter S, Allen ACB, Zoldan J, Sacks MS, Tunnell JW (2019) Non-destructive reflectance mapping of collagen fiber alignment in heart valve leaflets. Annals of Biomedical Engineering 47:1250-1264. doi:10.1007/s10439-019-02233-0

Goth W, Yang B, Lesicko J, Allen A, Sacks MS, Tunnell JW Polarized spatial frequency domain imaging of heart valve fiber structure. In: Proceedings of SPIE Volume 9710, Optical Elastography and Tissue Biomechanics III, 2016. p 971019. doi:10.1117/12.2212812

Gunning GM, Murphy BP (2015) Characterisation of the fatigue life, dynamic creep and modes of damage accumulation within mitral valve chordae tendineae. Acta Biomaterialia 24:193-200. doi:10.1016/j.actbio.2015.06.015

Horvat N, Virag L, Holzapfel GA, Sorić J, Karšaj I (2019) A finite element implementation of a growth and remodeling model for soft biological tissues: Verification and application to abdominal aortic aneurysms. Computer Methods in Applied Mechanics and Engineering 352:586-605. doi:10.1016/j.cma.2019.04.041

Hughes TJR (1987) The Finite Element Method: Linear Static and Dynamic Finite Element Analysis. Courier Corporation,

Jett SV et al. (2020) Integration of polarized spatial frequency domain imaging (pSFDI) with a biaxial mechanical testing system for quantification of load-dependent collagen architecture in soft collagenous tissues. Acta Biomaterialia 102:149-168. doi:10.1016/j.actbio.2019.11.028

Jett SV et al. (2018) An investigation of the anisotropic mechanical properties and anatomical structure of porcine atrioventricular heart valves. Journal of the Mechanical Behavior of Biomedical Materials 87:155-171. doi:10.1016/j.jmbbm.2018.07.024

Jimenez JH, Soerensen DD, He Z, He S, Yoganathan AP (2003) Effects of a saddle shaped annulus on mitral valve function and chordal force distribution: An *in vitro* study. Annals of Biomedical Engineering 31:1171-1181. doi:10.1114/1.1616929

Khoiy KA, Amini R (2016) On the biaxial mechanical response of porcine tricuspid valve leaflets. Journal of Biomechanical Engineering 138:104504. doi:10.1115/1.4034426

Klabunde R (2011) Cardiovascular Physiology Concepts. Lippincott Williams & Wilkins,

Konecky SD, Rice TB, Durkin AJ, Tromberg BJ (2011) Imaging scattering orientation with spatial frequency domain imaging. Journal of Biomedical Optics 16:126001

Kramer KE et al. (2019) An investigation of layer-specific tissue biomechanics of porcine atrioventricular heart valve leaflets. Acta Biomaterialia 96:368-384. doi:10.1016/j.actbio.2019.06.049

Lam JHC, Ranganathan N, Wigle ED, Silver MD (1970) Morphology of the human mitral valve. Circulation 41:449-458. doi:10.1161/01.CIR.41.3.449

Lee C-H, Carruthers CA, Ayoub S, Gorman RC, Gorman JH, III, Sacks MS (2015) Quantification and simulation of layer-specific mitral valve interstitial cells deformation under physiological loading. Journal of Theoretical Biology 373:26-39. doi:10.1016/j.jtbi.2015.03.004

Liao J, Priddy LB, Wang B, Chen J, Vesely I (2009) Ultrastructure of porcine mitral valve chordae tendineae. Journal of Heart Valve Disease 18:292

Liao J, Vesely I (2003) A structural basis for the size-related mechanical properties of mitral valve chordae tendineae. Journal of Biomechanics 36:1125-1133. doi:10.1016/S0021-9290(03)00109-X

Lim KO (1980) Mechanical properties and ultrastructure of normal human tricuspid valve chordae tendineae. Japanese Journal of Physiology 30:455-464. doi:10.2170/jjphysiol.30.455

Lim KO, Boughner DR (1975) Mechanical properties of human mitral valve chordae tendineae: Variation with size and strain rate. Canadian Journal of Physiology and Pharmacology 53:330-339. doi:10.1139/y75-048

Lim KO, Boughner DR (1976) Morphology and relationship to extensibility curves of human mitral valve chordae tendineae. Circulation Research 39:580-585. doi:10.1161/01.RES.39.4.580

Lim KO, Boughner DR (1977) Scanning electron microscopical study of human mitral valve chordae tendineae. Archives of Pathology and Laboratory Medicine 101:236-238

Lomholt M, Nielsen SL, Hansen SB, Andersen NT, Hasenkam JM (2002) Differential tension between secondary and primary mitral chordae in an acute in-vivo porcine model. Journal of Heart Valve Disease 11:337-345

Madhurapantula RS, Krell G, Morfin B, Roy R, Lister K, Orgel JPRO (2020) Advanced methodology and preliminary measurements of molecular and mechanical properties of heart valves under dynamic strain. International Journal of Molecular Sciences 21:763. doi:10.3390/ijms21030763

May-Newman K, Yin FC (1995) Biaxial mechanical behavior of excised porcine mitral valve leaflets. American Journal of Physiology: Heart and Circulatory Physiology 269:H1319-H1327. doi:10.1152/ajpheart.1995.269.4.H1319

Mazhar A, Saggese S, Pollins AC, Cardwell NL, Nanney LB, Cuccia DJ (2014) Noncontact imaging of burn depth and extent in a porcine model using spatial frequency domain imaging. Journal of Biomedical Optics 19:086019. doi:10.1117/1.JBO.19.8.086019

Meador WD et al. (2020) A detailed mechanical and microstructural analysis of ovine tricuspid valve leaflets. Acta Biomaterialia 102:100-113. doi:10.1016/j.actbio.2019.11.039

Millington-Sanders C, Meir A, Lawrence L, Stolinski C (1998) Structure of chordae tendineae in the left ventricle of the human heart. Journal of Anatomy 192:573-581. doi:10.1046/j.1469-7580.1998.19240573.x

Navia JL et al. (2010) Surgical management of secondary tricuspid valve regurgitation: Annulus, commissure, or leaflet procedure? Journal of Thoracic and Cardiovascular Surgery 139:1473-1482. e1475. doi:10.1016/j.jtcvs.2010.02.046

O'Leary SA, Doyle BJ, McGloughlin TM (2014) The impact of long term freezing on the mechanical properties of porcine aortic tissue. Journal of the Mechanical Behavior of Biomedical Materials 37:165-173. doi:10.1016/j.jmbbm.2014.04.015

Ogden RW (1972) Large deformation isotropic elasticity–on the correlation of theory and experiment for incompressible rubberlike solids. Proceedings of the Royal Society of London A Mathematical and Physical Sciences 326:565-584

Padala M, Sacks MS, Liou SW, Balachandran K, He Z, Yoganathan AP (2010) Mechanics of the mitral valve strut chordae insertion region. Journal of Biomechanical Engineering 132:081004. doi:10.1115/1.4001682

Pfannmüller B, Doenst T, Eberhardt K, Seeburger J, Borger MA, Mohr FW (2012) Increased risk of dehiscence after tricuspid valve repair with rigid annuloplasty rings. Journal of Thoracic and Cardiovascular Surgery 143:1050-1055. doi:10.1016/j.jtcvs.2011.06.019

Pokutta-Paskaleva A, Sulejmani F, DelRocini M, Sun W (2019) Comparative mechanical, morphological, and microstructural characterization of porcine mitral and tricuspid leaflets and chordae tendineae. Acta Biomaterialia 85:241-252. doi:10.1016/j.actbio.2018.12.029

Ritchie J, Jimenez J, He Z, Sacks MS, Yoganathan AP (2006) The material properties of the native porcine mitral valve chordae tendineae: An *in vitro* investigation. Journal of Biomechanics 39:1129-1135. doi:10.1016/j.jbiomech.2005.01.024

Ross CJ et al. (2020) Mechanics of porcine heart valves' strut chordae tendineae investigated as a leaflet–chordae–papillary muscle entity. Annals of Biomedical Engineering 48:1463-1474. doi:10.1007/s10439-020-02464-6

Sacks MS, David Merryman W, Schmidt DE (2009) On the biomechanics of heart valve function. Journal of Biomechanics 42:1804-1824. doi:10.1016/j.jbiomech.2009.05.015

Sacks MS, Smith DB, Hiester ED (1997) A small angle light scattering device for planar connective tissue microstructural analysis. Annals of Biomedical Engineering 25:678-689. doi:10.1007/BF02684845

Salvador L et al. (2008) A 20-year experience with mitral valve repair with artificial chordae in 608 patients. Journal of Thoracic and Cardiovascular Surgery 135:1280-1287.e1281. doi:10.1016/j.jtcvs.2007.12.026

Sedransk KL, Grande-Allen KJ, Vesely I (2002) Failure mechanics of mitral valve chordae tendineae. Journal of Heart Valve Disease 11:644-650

Seeburger J et al. (2014) Off-pump transapical implantation of artificial neo-chordae to correct mitral regurgitation: the TACT Trial (Transapical Artificial Chordae Tendinae) proof of concept. Journal of the American College of Cardiology 63:914-919. doi:10.1016/j.jacc.2013.07.090

Silver MD, Lam JHC, Ranganathan N, Wigle ED (1971) Morphology of the human tricuspid valve. Circulation 43:333-348. doi:10.1161/01.CIR.43.3.333

Stemper BD, Yoganandan N, Stineman MR, Gennarelli TA, Baisden JL, Pintar FA (2007) Mechanics of fresh, refrigerated, and frozen arterial tissue. Journal of Surgical Research 139:236-242. doi:10.1016/j.jss.2006.09.001

Storn R, Price K (1997) Differential evolution–A simple and efficient heuristic for global optimization over continuous spaces. Journal of Global Optimization 11:341-359. doi:10.1023/A:1008202821328

Stuge O, Liddicoat J (2006) Emerging opportunities for cardiac surgeons within structural heart disease. Journal of Thoracic and Cardiovascular Surgery 132:1258-1261. doi:10.1016/j.jtcvs.2006.08.049

Toma M, Jensen MØ, Einstein DR, Yoganathan AP, Cochran RP, Kunzelman KS (2016) Fluid–structure interaction analysis of papillary muscle forces using a comprehensive mitral valve model with 3D chordal structure. Annals of Biomedical Engineering 44:942-953

Venkatasubramanian RT, Grassl ED, Barocas VH, Lafontaine D, Bischof JC (2006) Effects of freezing and cryopreservation on the mechanical properties of arteries. Annals of Biomedical Engineering 34:823-832. doi:10.1007/s10439-005-9044-x

Waller BF, Howard J, Fess S (1994) Pathology of mitral valve stenosis and pure mitral regurgitation—Part I. Clinical Cardiology 17:330-336. doi:10.1002/clc.4960170611

Waller BF, Howard J, Fess S (1995) Pathology of tricuspid valve stenosis and pure tricuspid regurgitation—Part I. Clinical Cardiology 18:97-102. doi:10.1002/clc.4960180212

Zuo K, Pham T, Li K, Martin C, He Z, Sun W (2016) Characterization of biomechanical properties of aged human and ovine mitral valve chordae tendineae. Journal of the Mechanical Behavior of Biomedical Materials 62:607-618. doi:10.1016/j.jmbbm.2016.05.034

List of Tables

Table 1 – Quantified collagen fiber architecture, including the predicted collagen fiber orientation angle θ_{fiber} and the predicted degree of optical anisotropy (DOA), for the CT segments (see **Fig. 1b**). Values are reported as mean±SEM.

		Loading Point					
		0	1	2	3	4	5
TVAL	θ_{fiber}	65.6±2.3°	66.5±1.9°	66.6±1.8°	66.1±1.7°	66.1±2.1°	64.4±1.3°
(n=7)	DOA	0.14±0.01	0.15±5E-3	0.16±0.01	0.17±0.01	0.17±0.01	0.20±0.01
MVAL	θ_{fiber}	71.9±3.0°	72.3±2.8°	72.1±2.9°	72.4±2.9°	73.9±3.6°	72.7±3.3°
(n=7)	DOA	0.09±0.01	0.09±0.01	0.10±0.01	0.11±0.01	0.13±0.02	0.15±0.01

Note: Variations in the number of specimens were due to limitations with the camera field of view not allowing a full visibility of the ROIs within the polarizer lens window.

Table 2 – Percentage changes in the predicted degree of optical anisotropy (DOA) between two consecutive states of the 5 loading points for the CT segments (see **Fig. 1b**). Values are reported as mean±SEM, and p-values determined from the one-way ANOVA are given in square brackets.

TVAL Strut Chordae Tendineae ROI (n=7)					
Loading Point	Loading Point as the Reference (Baseline)				
	0	1	2	3	4
0	–	–	–	–	–
1	7.1±4.7% [0.932]	–	–	–	–
2	10.7±7.8% [0.622]	3.6±5.6% [0.987]	–	–	–
3	16.1±6.8% [0.195]	9.1±3.8% [0.712]	5.5±2.3% [0.968]	–	–
4	15.7±6.8% [0.214]	8.7±3.3% [0.741]	5.0±4.0% [0.976]	-0.5±2.6% [1.000]	–
5	35.6±7.0% [1E-5]*	28.9±4.5% [2E-4]*	25.3±4.2% [0.002]*	19.9±3.1% [0.013]*	20.4±2.6% [0.012]*
MVAL Strut Chordae Tendineae ROI (n=7)					
Loading Point	Loading Point as the Reference (Baseline)				
	0	1	2	3	4
0	–	–	–	–	–
1	0.3±3.1% [1.000]	–	–	–	–
2	8.7±6.0% [0.993]	8.4±4.3% [0.996]	–	–	–
3	22.5±5.6% [0.790]	22.3±4.0% [0.821]	13.9±3.5% [0.976]	–	–
4	35.1±11.4% [0.167]	35.0±10.3% [0.187]	26.6±11.5% [0.420]	13.3±9.5% [0.851]	–
5	46.4±8.7% [0.036]*	46.3±7.5% [0.042]*	38.3±7.5% [0.126]	25.0±5.1% [0.444]	11.4±5.5% [0.982]

Note: Variations in the number of specimens were due to limitations with the camera field of view not allowing a full visibility of the ROIs within the polarizer lens window.

* statistically-significant changes (p<0.05).

Table 3 – Quantified collagen fiber architecture, including the predicted collagen fiber orientation angle θ_{fiber} and the predicted degree of anisotropy (DOA), for the CT-leaflet insertions (see **Fig. 1b**). Values are reported as mean±SEM.

		Loading Point					
		0	1	2	3	4	5
TVAL	θ_{fiber}	73.7±2.4°	73.2±2.3°	72.6±2.7°	70.9±2.3°	70.5±2.1°	68.6±1.75°
(n=8)	DOA	0.13±0.01	0.14±0.01	0.14±0.01	0.15±0.01	0.15±0.01	0.19±0.01
MVAL	θ_{fiber}	78.2±1.8°	78.0±1.7°	77.9±1.9°	78.2±1.5°	78.1±1.6°	76.6±2.0°
(n=10)	DOA	0.11±4E-3	0.11±5E-3	0.12±5E-3	0.13±0.01	0.14±0.01	0.16±0.01

Note: Variations in the number of specimens were due to limitations with the camera field of view not allowing a full visibility of the ROIs within the polarizer lens window.

Table 4 – Percentage changes in the predicted degree of optical anisotropy (DOA) between two consecutive states of the 5 loading points for the CT-leaflet insertions (see **Fig. 1b**). Value are reported as mean±SEM, and p-values, determined from the one-way ANOVA, are given in square brackets.

TVAL Strut CT-Leaflet Insertion (n=8)					
Loading Point	Loading Point as the Reference (Baseline)				
	0	1	2	3	4
0	–	–	–	–	–
1	7.4±1.2% [0.980]	–	–	–	–
2	12.7±2.1% [0.833]	5.3±2.0% [0.996]	–	–	–
3	18.6±2.6% [0.393]	11.2±2.2% [0.821]	5.9±1.6% [0.976]	–	–
4	19.9±2.6% [0.345]	12.5±2.1% [0.774]	7.2±2.1% [0.961]	1.3±1.2% [1.000]	–
5	37.7±4.0% [0.001]*	30.5±3.8% [0.009]*	25.3±3.7% [0.032]*	19.6±2.7% [0.171]	18.3±2.6% [0.202]
MVAL Strut CT-Leaflet Insertion (n=10)					
Loading Point	Loading Point as the Reference (Baseline)				
	0	1	2	3	4
0	–	–	–	–	–
1	3.2±2.5% [0.996]	–	–	–	–
2	7.5±3.4% [0.855]	4.4±1.8% [0.985]	–	–	–
3	17.3±2.8% [0.071]	14.2±2.6% [0.205]	9.9±2.5% [0.567]	–	–
4	22.2±3.5% [0.006]*	19.1±3.0% [0.024]*	14.7±2.9% [0.119]	4.9±1.4% [0.938]	–
5	37.5±2.8% [1E-7]*	34.4±2.5% [8E-7]*	30.2±2.4% [9E-6]*	20.5±2.7% [0.003]*	15.6±2.4% [0.004]*

Note: Variations in the number of specimens were due to limitations with the camera field of view not allowing a full visibility of the ROIs within the polarizer lens window.

* statistically-significant changes (p<0.05).

Table 5 – Regional analyses of the quantified collagen fiber architecture for the TVAL CT-leaflet insertion (n=8, see **Fig. 1e**). Values are reported as mean±SEM.

	Quantified Collagen Fiber Orientation Angle (θ_{fiber})					
Loading Point	0	1	2	3	4	5
Sub-region 1	77.3±3.5°	77.5±2.9°	77.1±3.4°	77.3±3.0°	75.4±3.1°	72.4±2.8°
Sub-region 2	68.2±2.9°	68.4±2.6°	67.6±3.3°	67.0±2.9°	64.6±3.1°	64.1±2.3°
Sub-region 3	64.9±2.9°	62.5±2.7°	64.4±2.8°	60.7±2.1°	66.6±3.2°	61.4±2.0°
Sub-region 4	86.3±2.5°	86.4±2.3°	85.8±3.2°	85.0±3.0°	83.5±3.5°	80.9±3.0°
Sub-region 5	69.7±3.4°	69.0±3.2°	67.8±2.8°	66.3±3.4°	65.6±3.3°	64.9±2.2°
Sub-region 6	65.1±4.7°	63.9±4.9°	66.5±6.4°	63.9±4.8°	63.1±4.0°	61.8±3.0°
Sub-region 7	89.6±2.6°	89.9±2.5°	87.7±2.9°	86.3±2.3°	85.0±2.3°	83.6±2.3°
Sub-region 8	72.2±2.9°	71.9±2.9°	70.0±2.4°	69.5±3.4°	69.2±3.3°	68.3±2.9°
Sub-region 9	69.7±4.4°	69.1±5.6°	66.8±5.4°	62.4±5.1°	61.2±3.8°	60.3±2.3°
	Quantified Degree of Optical Alignment (DOA)					
Loading Point	0	1	2	3	4	5
Sub-region 1	0.11±0.01	0.12±0.01	0.13±0.01	0.14±0.01	0.15±0.01	0.18±0.01
Sub-region 2	0.16±0.01	0.17±0.01	0.17±0.01	0.18±0.01	0.18±0.01	0.23±0.02
Sub-region 3	0.12±0.01	0.14±0.01	0.13±0.01	0.16±0.01	0.14±0.01	0.18±0.02
Sub-region 4	0.11±0.01	0.12±0.01	0.13±0.01	0.14±0.01	0.14±0.01	0.17±0.01
Sub-region 5	0.15±0.01	0.16±0.01	0.17±0.01	0.17±0.01	0.18±0.01	0.22±0.01
Sub-region 6	0.12±0.01	0.13±0.01	0.13±0.01	0.14±0.02	0.13±0.02	0.16±0.02
Sub-region 7	0.10±0.01	0.11±0.01	0.12±0.01	0.13±0.01	0.13±0.01	0.14±0.02
Sub-region 8	0.14±0.01	0.15±0.01	0.16±0.01	0.16±0.01	0.18±0.01	0.22±0.01
Sub-region 9	0.12±0.01	0.13±0.01	0.14±0.01	0.15±0.01	0.15±0.01	0.18±0.02

Note: Variations in the number of specimens were due to limitations with the camera field of view not allowing a full visibility of the ROIs within the polarizer lens window.

Table 6 – Regional analyses of the quantified collagen fiber architecture for the MVAL CT-leaflet insertion (n=10, see **Fig. 1e**). Values are reported as mean±SEM.

	Quantified Collagen Fiber Orientation Angle (θ_{fiber})					
Loading Point	0	1	2	3	4	5
Sub-region 1	82.2±2.8°	83.1±2.8°	83.1±2.5°	83.7±2.7°	84.0±2.9°	83.3±2.6°
Sub-region 2	72.6±3.2°	73.0±3.3°	73.3±3.3°	73.1±3.3°	73.0±3.5°	73.6±3.6°
Sub-region 3	68.2±1.9°	67.6±1.6°	66.2±2.0°	69.3±3.5°	69.6±3.2°	67.0±3.3°
Sub-region 4	93.3±1.5°	92.6±1.5°	92.6±1.8°	92.6±1.2°	91.2±1.6°	89.9±1.4°
Sub-region 5	73.3±3.6°	71.6±3.4°	73.0±3.3°	73.0±3.3°	72.3±3.4°	72.8±3.3°
Sub-region 6	65.9±2.3°	68.4±3.4°	67.1±3.3°	66.5±4.1°	67.9±4.0°	66.9±3.1°
Sub-region 7	100.2±2.9°	101.9±1.6°	100.3±1.8°	99.8±2.1°	98.0±1.7°	95.2±2.0°
Sub-region 8	80.0±4.3°	77.1±4.0°	78.5±4.2°	77.7±4.0°	77.0±3.3°	73.6±3.1°
Sub-region 9	67.8±2.9°	66.5±2.3°	67.3±3.2°	67.7±3.1°	69.5±2.8°	67.5±2.6°
	Quantified Degree of Optical Alignment (DOA)					
Loading Point	0	1	2	3	4	5
Sub-region 1	0.10±0.01	0.10±0.01	0.11±0.01	0.13±0.01	0.13±0.01	0.14±0.01
Sub-region 2	0.12±0.01	0.13±0.01	0.14±0.01	0.16±0.01	0.17±0.01	0.20±0.01
Sub-region 3	0.11±0.01	0.12±0.01	0.12±0.01	0.14±0.01	0.15±0.01	0.18±0.01
Sub-region 4	0.11±0.01	0.11±0.01	0.11±0.01	0.12±0.01	0.13±0.01	0.14±0.01
Sub-region 5	0.14±0.01	0.14±0.01	0.15±0.01	0.16±0.01	0.17±0.01	0.21±0.01
Sub-region 6	0.12±0.01	0.12±0.01	0.13±0.01	0.14±0.01	0.15±0.01	0.18±0.01
Sub-region 7	0.09±0.01	0.09±0.01	0.09±0.01	0.10±0.01	0.11±0.01	0.11±0.01
Sub-region 8	0.11±0.01	0.11±3E-3	0.12±3E-3	0.12±3E-3	0.13±0.01	0.16±3E-3
Sub-region 9	0.10±0.01	0.10±0.01	0.11±0.01	0.12±0.01	0.12±0.01	0.14±0.01

Note: Variations in the number of specimens was due to limitations with the camera field of view not allowing a full visibility of the ROIs within the polarizer lens window.

Table 7 – Percentage changes in the predicted degree of optical anisotropy (DOA) between two non-sequential loading states for sub-regions of the CT-leaflet insertion (see **Fig. 1e**). Values are reported as mean±SEM, and p-values are determined from the one-way ANOVA and multiple comparisons are given in square brackets.

	TVAL strut CT-Leaflet Insertion (n=8)		MVAL strut CT-Leaflet Insertion (n=10)	
	Loading Point 0 → Loading Point 5	Loading Point 2 → Loading Point 5	Loading Point 0 → Loading Point 5	Loading Point 2 → Loading Point 5
Sub-region 1	46.3±6.2% [0.015]*	36.0±7.8% [0.233]	25.6±7.6% [0.025]*	28.0±7.1% [0.184]
Sub-region 2	41.2±6.2% [0.006]*	50.1±4.8% [0.053]	37.3±2.6% [1E-7]*	30.0±3.1% [2E-5]*
Sub-region 3	33.0±15.0%	48.5±5.6%	43.1±5.7% [3E-5]*	22.9±11.9% [2E-4]*
Sub-region 4	41.1±6.1% [0.008]*	22.6±4.6% [0.234]	20.7±4.8% [0.119]	23.2±4.0% [0.150]
Sub-region 5	38.3±2.9% [0.008]*	41.8±3.6% [0.087]	31.3±2.3% [5E-8]*	26.7±2.5% [8E-6]*
Sub-region 6	31.8±6.5%	38.2±3.7%	34.6±4.7% [0.008]*	22.0±7.7% [0.023]*
Sub-region 7	25.2±6.0%	17.1±5.9%	14.8±5.7%	12.9±5.6%
Sub-region 8	39.2±3.9% [2E-5]*	41.0±5.1% [6E-4]*	31.3±2.5% [2E-8]*	30.0±3.6% [8E-7]*
Sub-region 9	33.7±6.0% [0.003]*	29.9±7.7% [0.071]	22.3±4.0%	22.1±5.9%

Note: Variations in the number of specimens were due to limitations with the camera field of view not allowing a full visibility of the ROIs within the polarizer lens window. In addition, entries without p-values indicate that multiple comparisons were not performed, as the initial ANOVA was insignificant.

* statistically-significant changes (p<0.05).
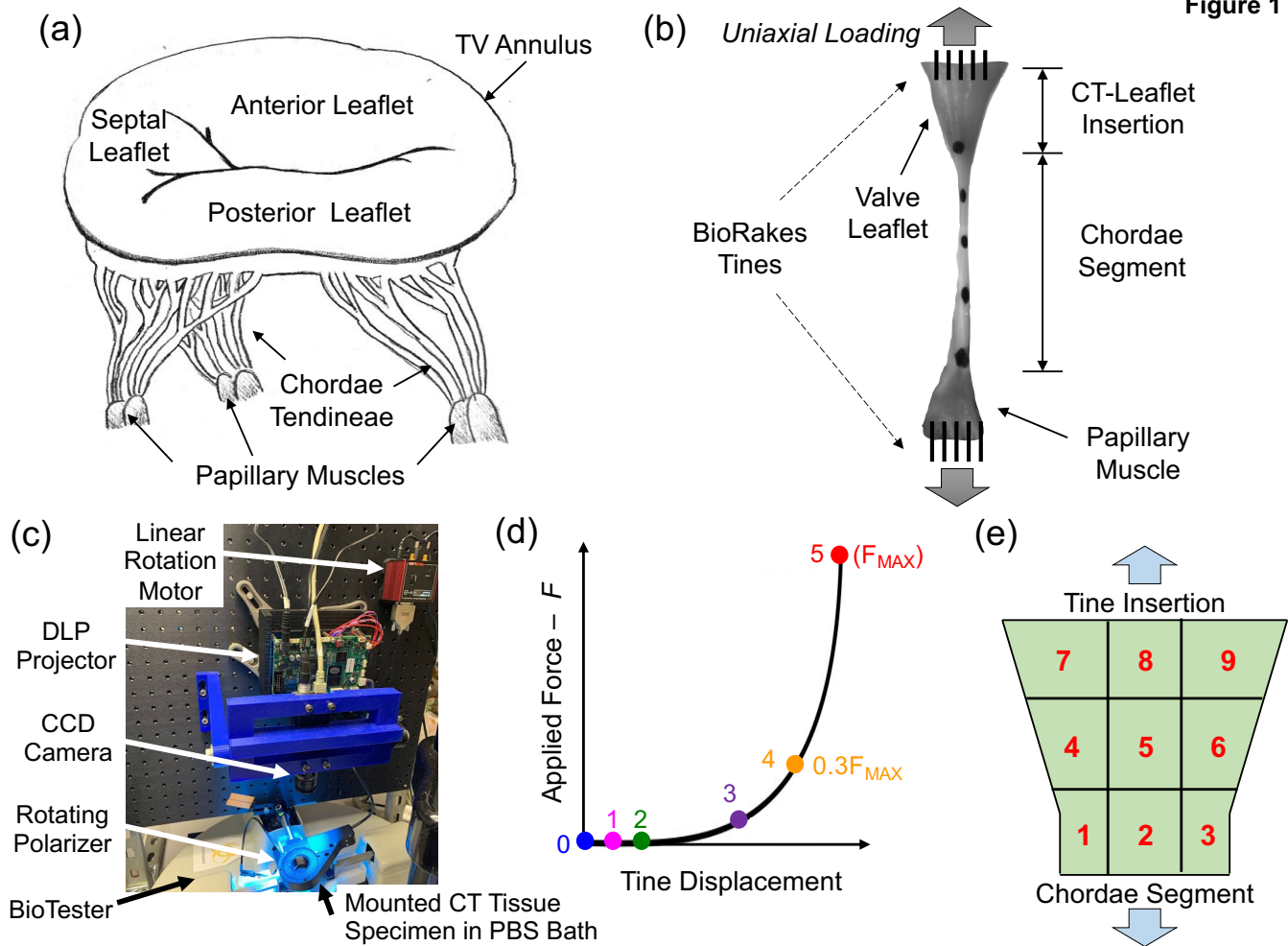
Figure 1 – (a) Illustration of a tricuspid valve and its sub-valvular components. (b) Schematic of the leaflet-strut CT-papillary muscle entity-based tissue specimen dissected from porcine mitral valves and tricuspid valves under investigation. (c) Integrated instrument for conducting uniaxial mechanical testing and collagen fiber microstructural quantification. (d) Six loading points defined along the force-displacement curve for acquiring load-dependent CFAs. (e) Schematic of the sub-regions for analyzing the regional variations in the quantified CFAs for the CT-leaflet insertion.

Figure 2
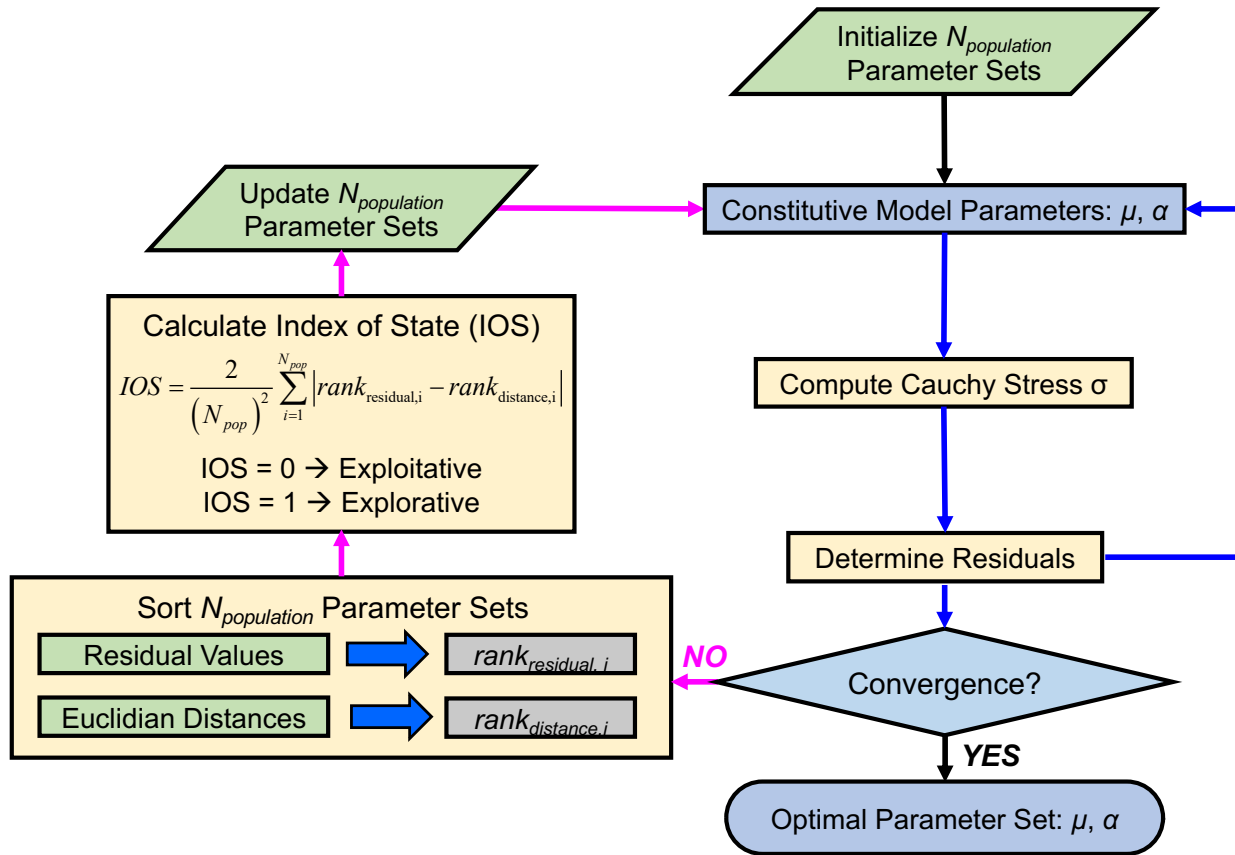
Figure 2 – Algorithmic flowchart for the differential evolution optimization framework used in determining the Ogden-type constitutive model parameters.

Figure 3
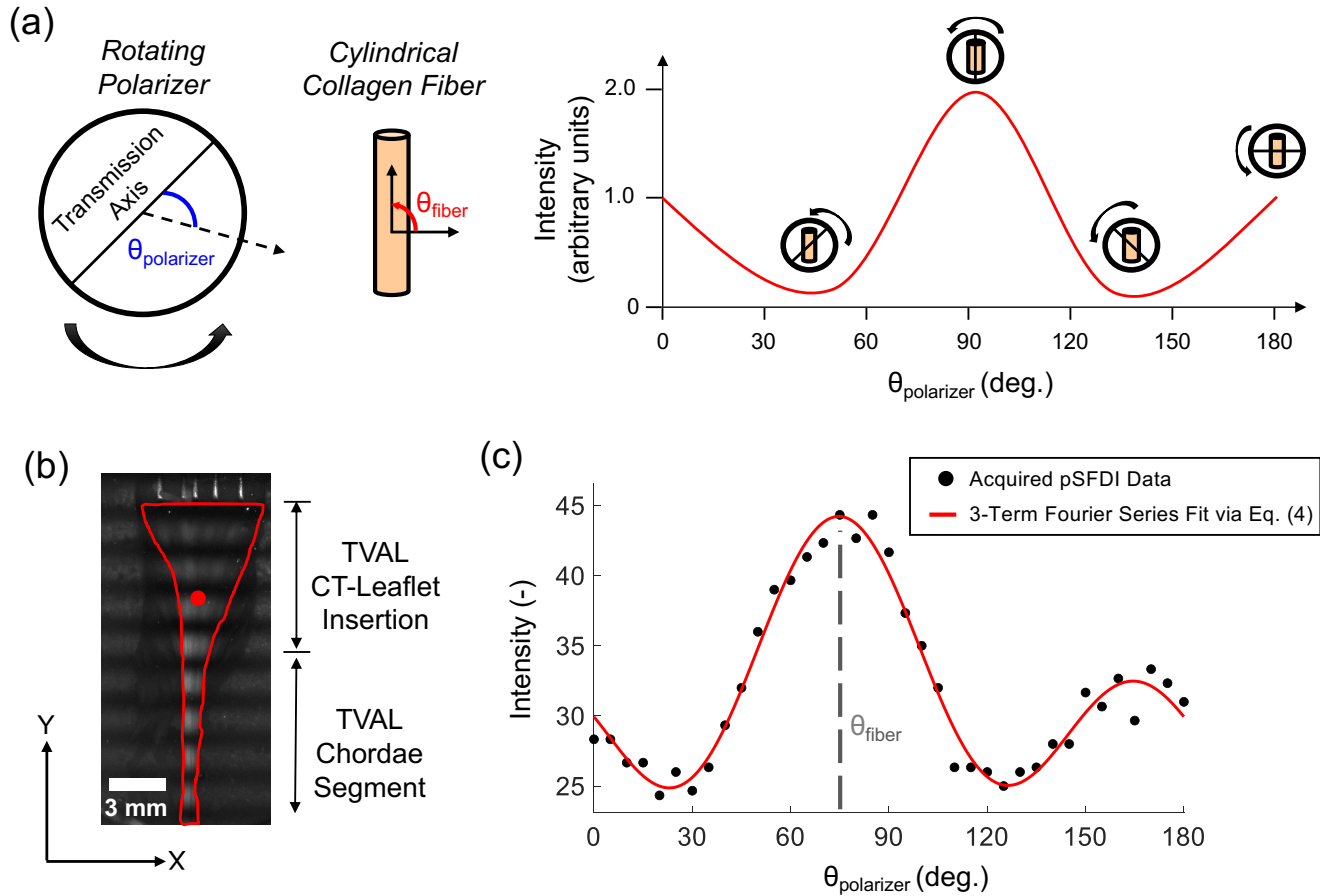
Figure 3 – (a) Illustration of the birefringent reflected light intensity versus polarizer angle $\theta_{polarizer}$ for an example of a (cylindrical) collagen fiber with an orientation angle θ_{fiber}=90°, where the maximum intensity occurs when $\theta_{polarizer}$ and θ_{fiber} match each other. (b) pSFDI image from a representative TVAL strut CT-leaflet insertion, with the region of interest (ROI) of the tissue outlined in red, together with a selected pixel (red circle). (c) Measured reflected light intensity versus $\theta_{polarizer}$ from the analyzed pixel (red circle in (b)), superimposed with the 3-term Fourier series fit that shows how θ_{fiber} was determined.

Figure 4
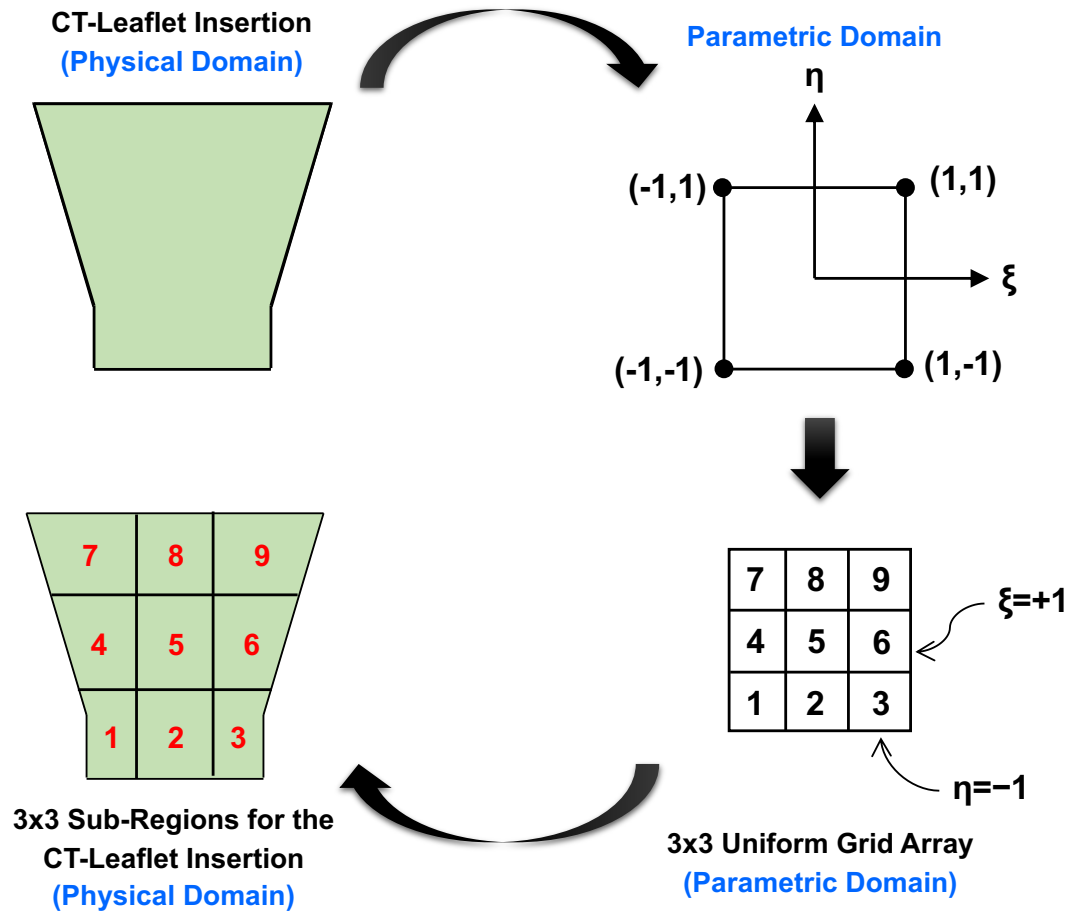
Figure 4 – Schematic of the procedure for generating the sub-regions for the regional analysis of the load-dependent CFAs of the CT-leaflet insertions. The isoparametric mapping concept in the finite element methods was adopted, and the uniform 3x3 grid was generated in the parametric domain and mapped back to the CT-leaflet insertion in the physical domain.

Figure 5
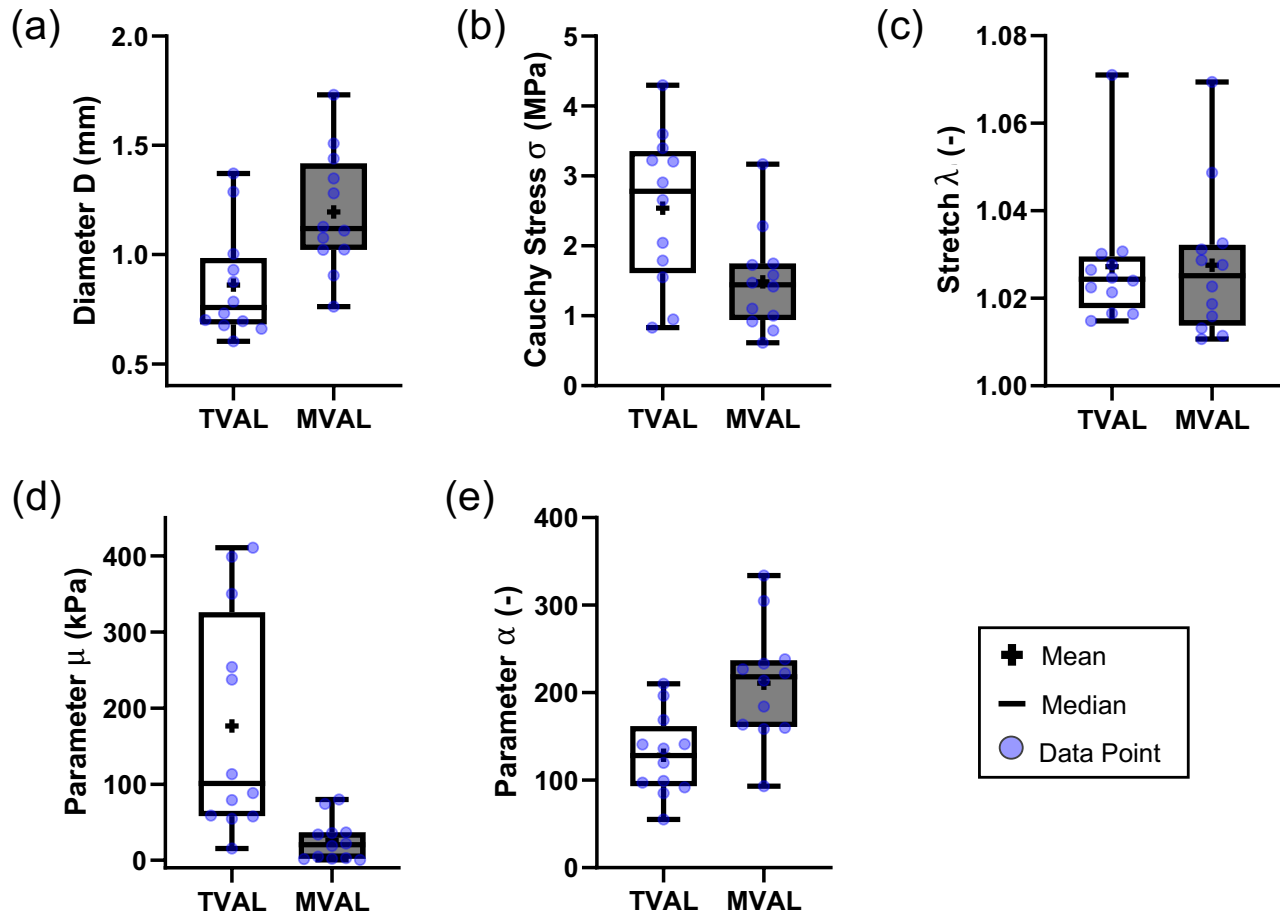
Figure 5 – Whisker box plots for (a) the thickness D, (b) the Cauchy stress σ, (c) the tissue stretch λ, and (d-e) the Ogden model parameters, μ and α, for the TVAL and MVAL CT segments. Tissue thickness D was obtained at the unloaded state Ω_0, whereas the mechanical testing quantities and the constitutive parameters (i.e., σ, λ, μ, and α) were determined at peak load F_{max} with respect to the post-preconditioning configuration Ω_1.
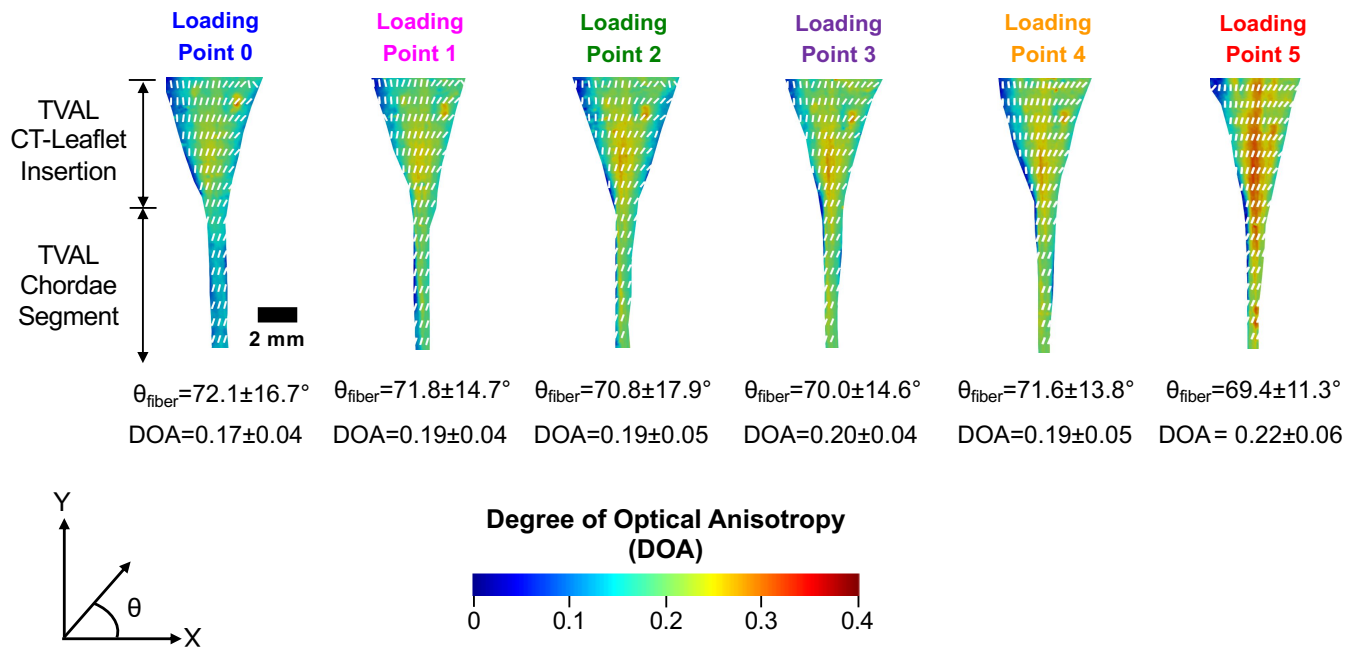
Figure 6

Figure 6 – Progressive CFAs of a representative TVAL strut chordae entity specimen under uniaxial mechanical testing (~38,000 pixels in the analyzed region). The white lines represent the predicted collagen fiber orientations of the selected coarser pixels (for visualization purpose), and the colormap intensities signify the degree of optical anisotropy (DOA). Values of the predicted θ_{fiber} and DOA are presented as mean±SEM.

Figure 7
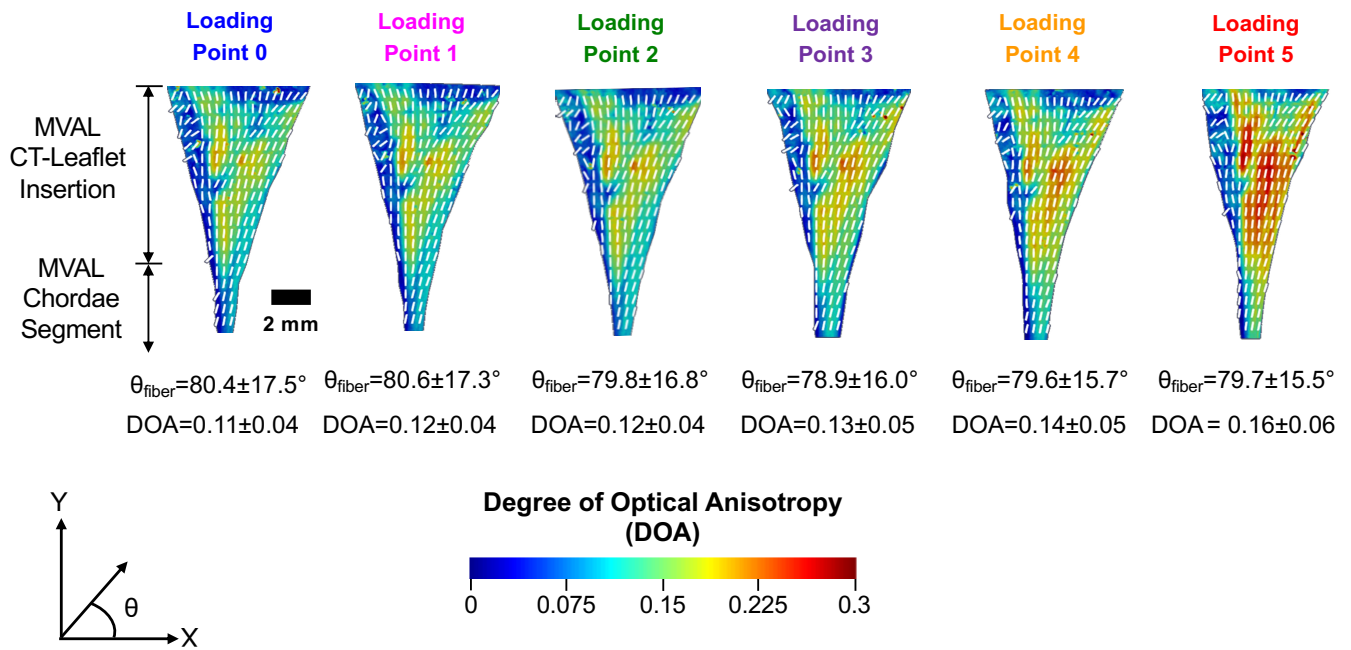
Figure 7 – Progressive CFAs of a representative MVAL strut chordae entity specimen under uniaxial mechanical testing (~15,000 pixels in the analyzed region). The white lines represent the predicted collagen fiber orientations of selected coarser pixels (for visualization purpose), and the colormap intensities signify the degree of optical anisotropy (DOA). Values of the predicted θ_{fiber} and DOA are presented as mean±SEM.
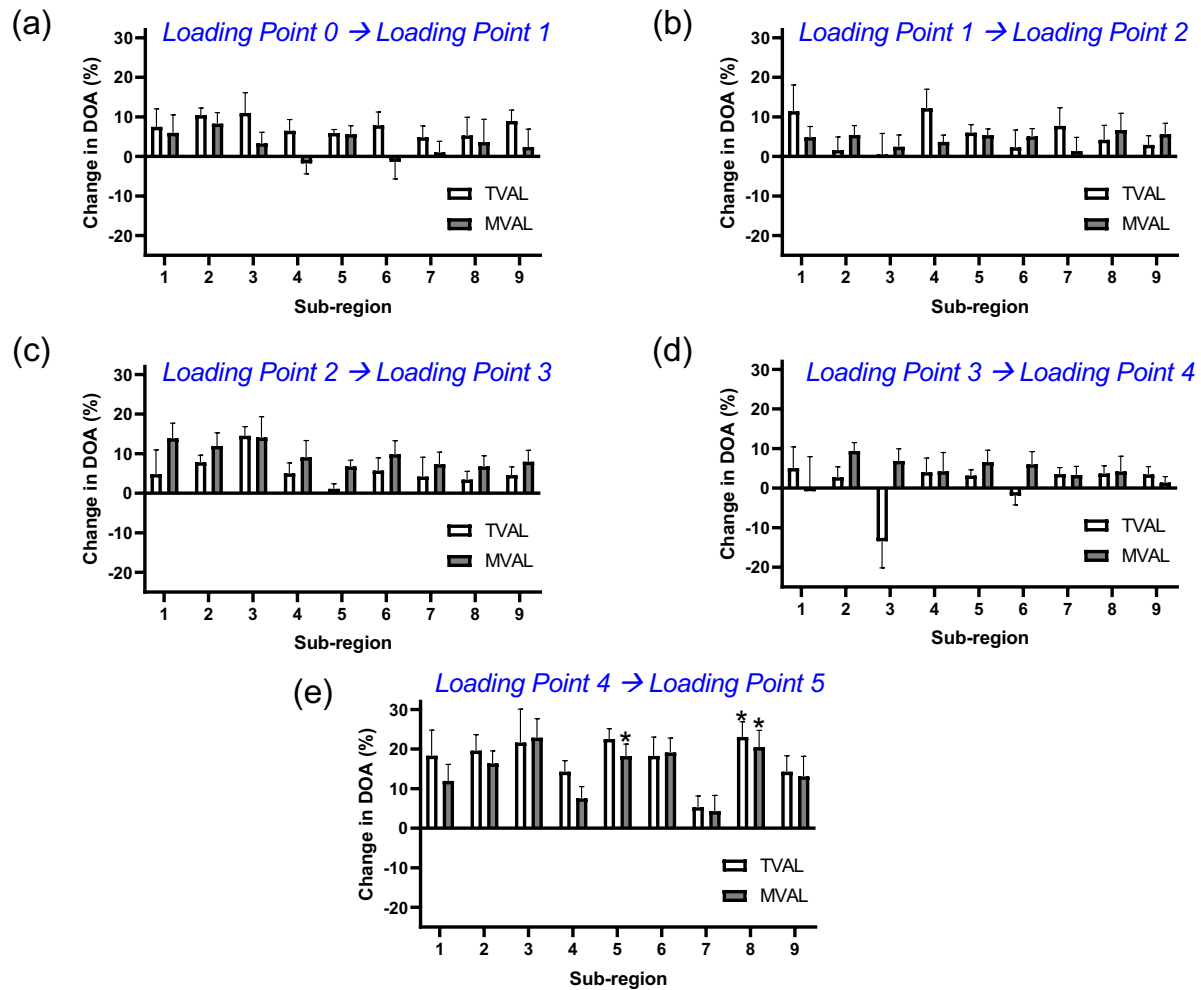
Figure 8 – Comparison of the predicted DOAs of the CT-leaflet insertions between the sequential loading points based on the 3x3 sub-regional analysis: (a) Loading Points 0 vs. 1, (b) Loading Points 1 vs. 2, (c) Loading Points 2 vs. 3, (d) Loading Points 3 vs. 4, and (e) Loading Points 4 vs. 5. Values are presented as mean±SEM, and * denotes a statistically significant change (p<0.05).

Supplementary Material

This Supplementary Material section contains quantile-quantile (QQ) plots for the manuscript "*Quantification of load-dependent changes in the collagen fiber architecture for strut chordae tendineae-leaflet insertion of porcine atrioventricular heart valves*". The QQ plots demonstrate the dispersion of the predicted collagen fiber orientation angle θ_{fiber} and the quantified degree of optical anisotropy (DOA) for the TVAL strut chordae segments (**Figs. S1-S2**), the MVAL strut chordae segments (**Figs. S3-S4**), the TVAL strut CT-leaflet insertions (**Figs. S5-S6**), and the MVAL strut CT-leaflet insertions (**Figs. S7-S8**).
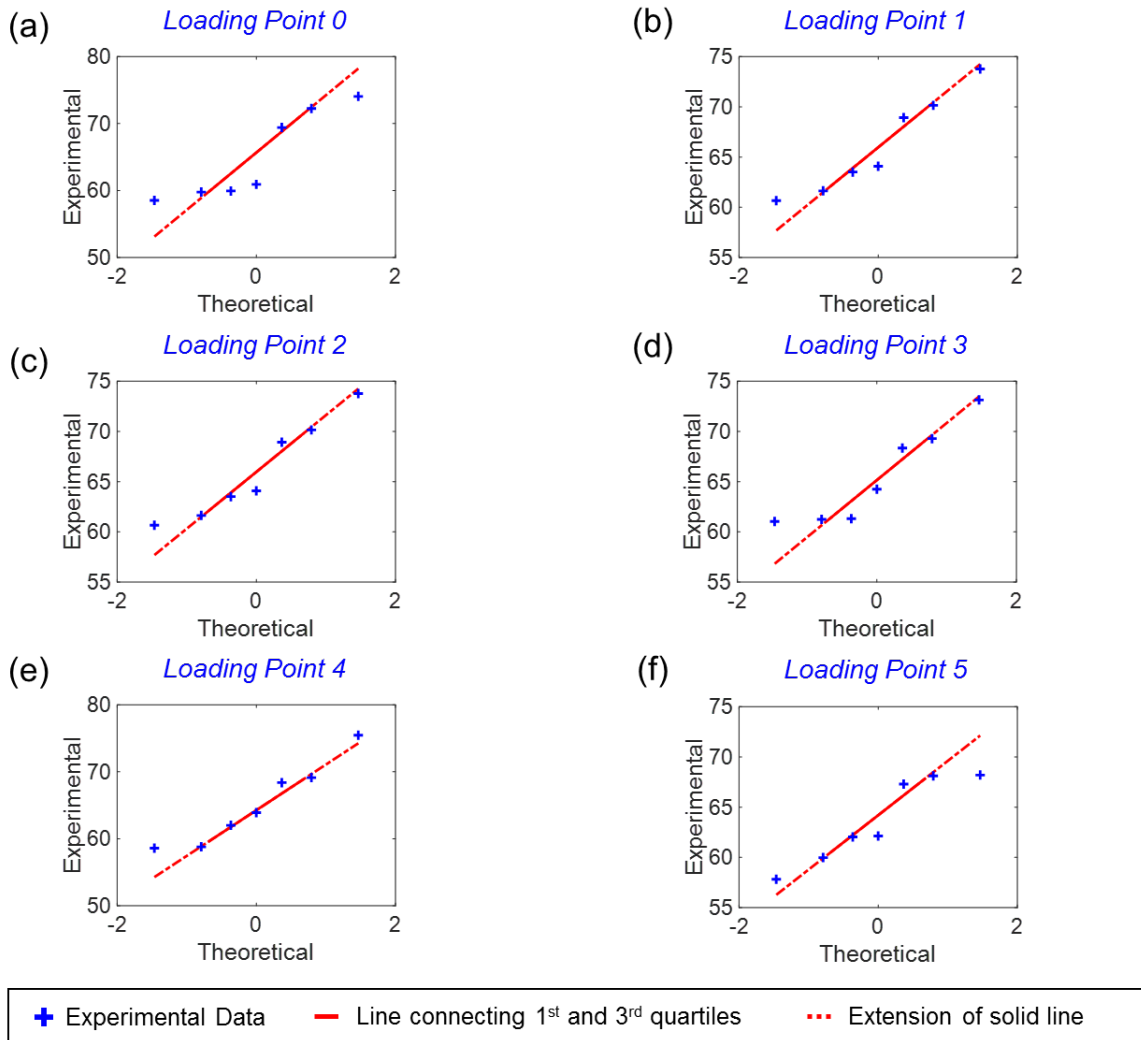
Figure S1 – Quantile-Quantile (QQ) plot for the predicted θ_{fiber} – TVAL strut chordae segments, considering various loading conditions: (a)-(f) Loading Points 0-5.
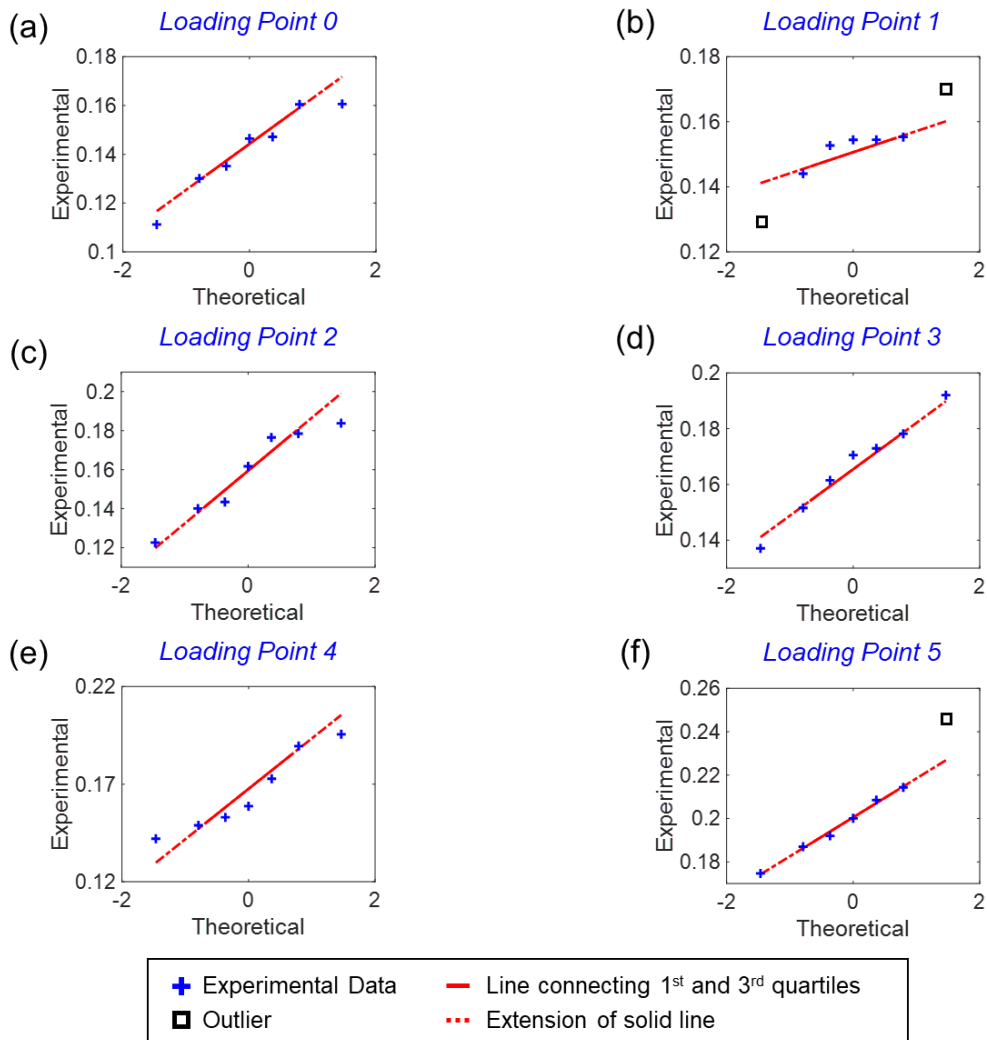
Figure S2 – Quantile-Quantile (QQ) plot for the quantified degree of optical anisotropy (DOA) – TVAL strut chordae segments, considering various loading conditions: (a)-(f) Loading Points 0-5.
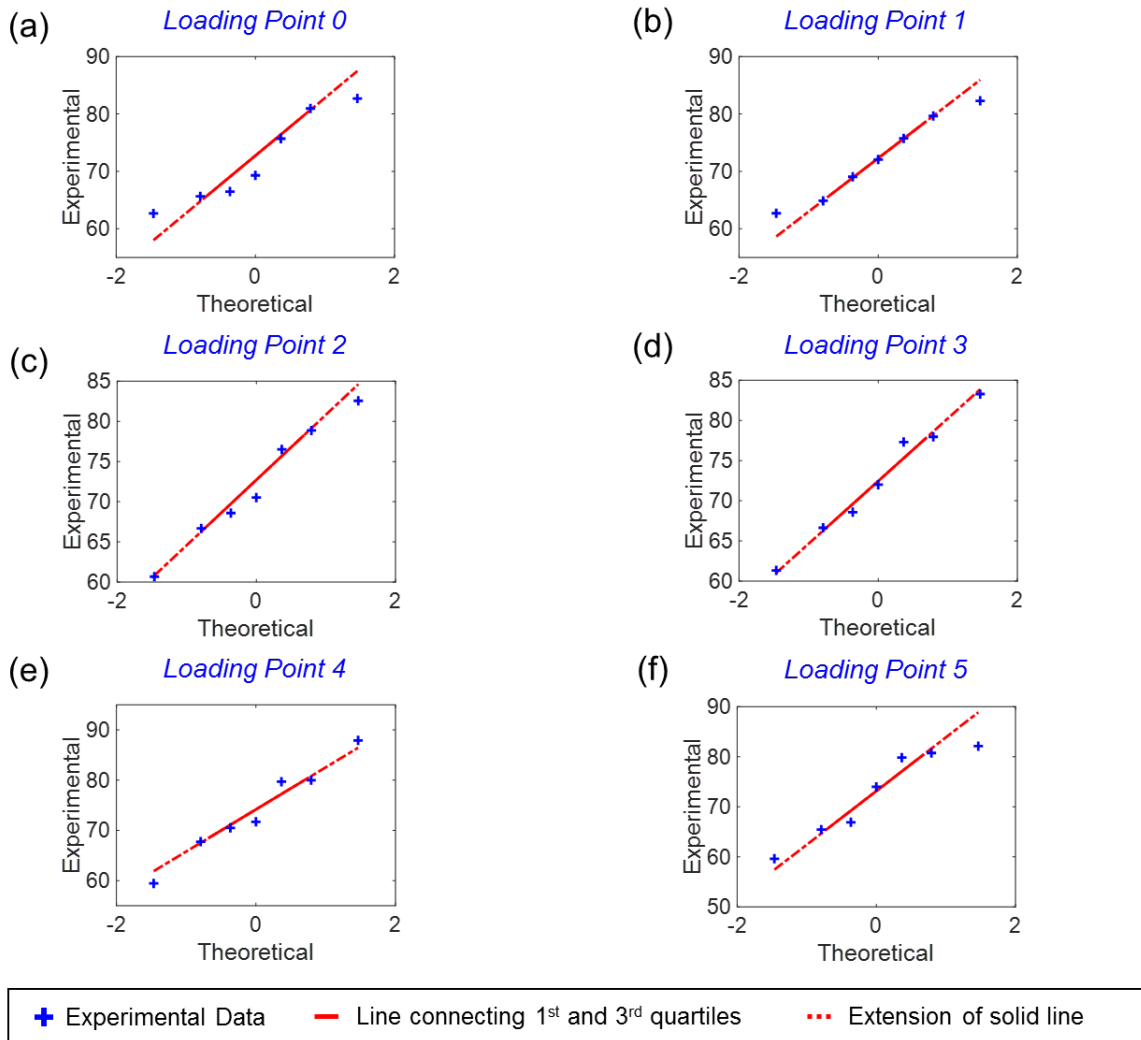
Figure S3 – Quantile-Quantile (QQ) plot for the predicted θ_{fiber} – MVAL strut chordae segments, considering various loading conditions: (a)-(f) Loading Points 0-5.
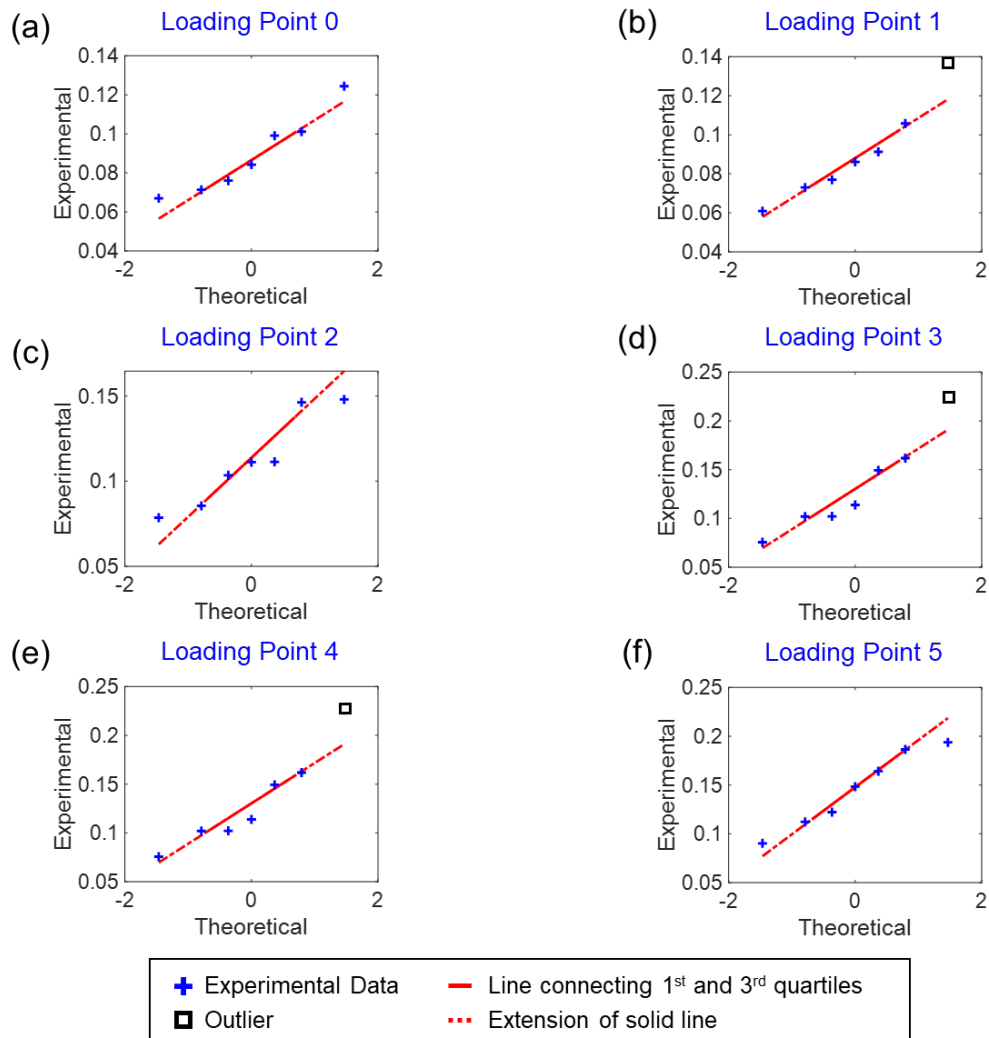
Figure S4 – Quantile-Quantile (QQ) plot for the quantified degree of optical anisotropy (DOA) – MVAL strut chordae segments, considering various loading conditions: (a)-(f) Loading Points 0-5.
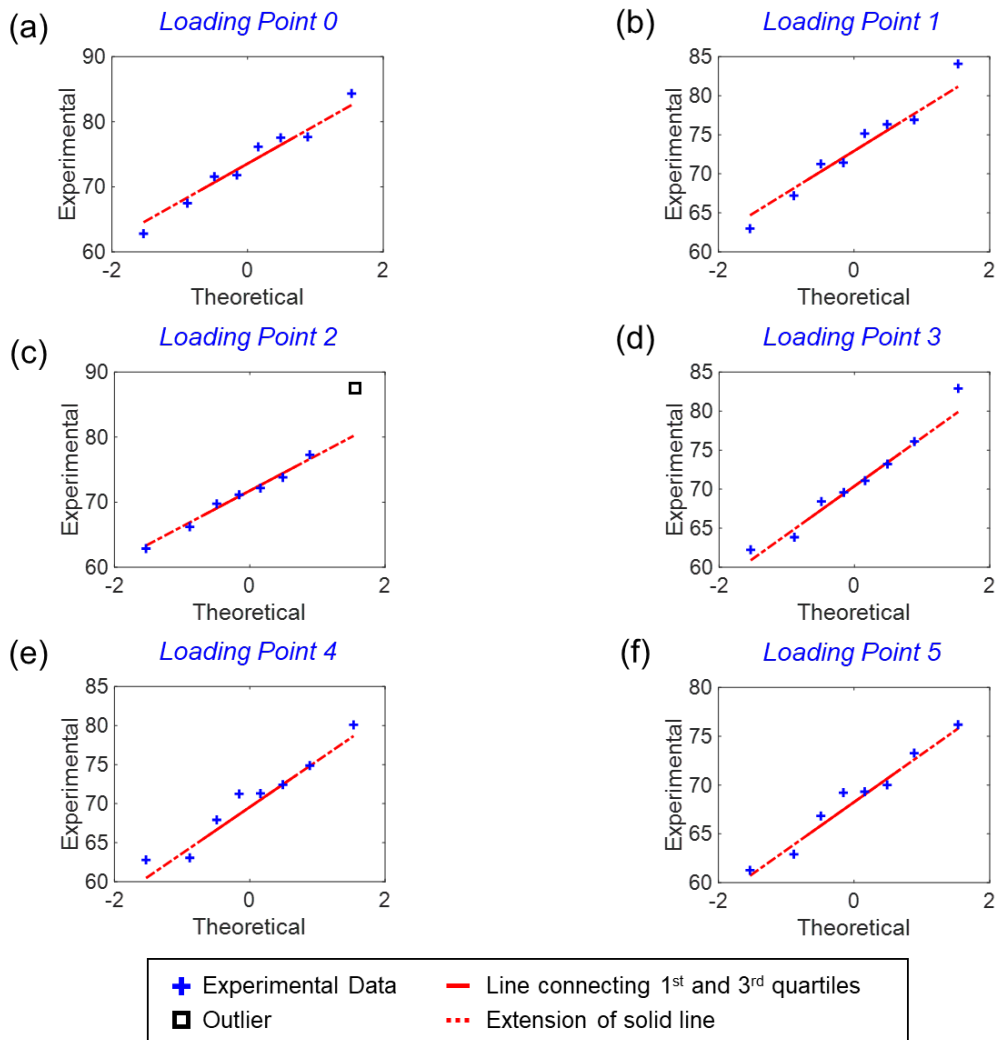
Figure S5 – Quantile-Quantile (QQ) plot for the predicted θ_{fiber} – TVAL strut CT-leaflet insertions, considering various loading conditions: (a)-(f) Loading Points 0-5.
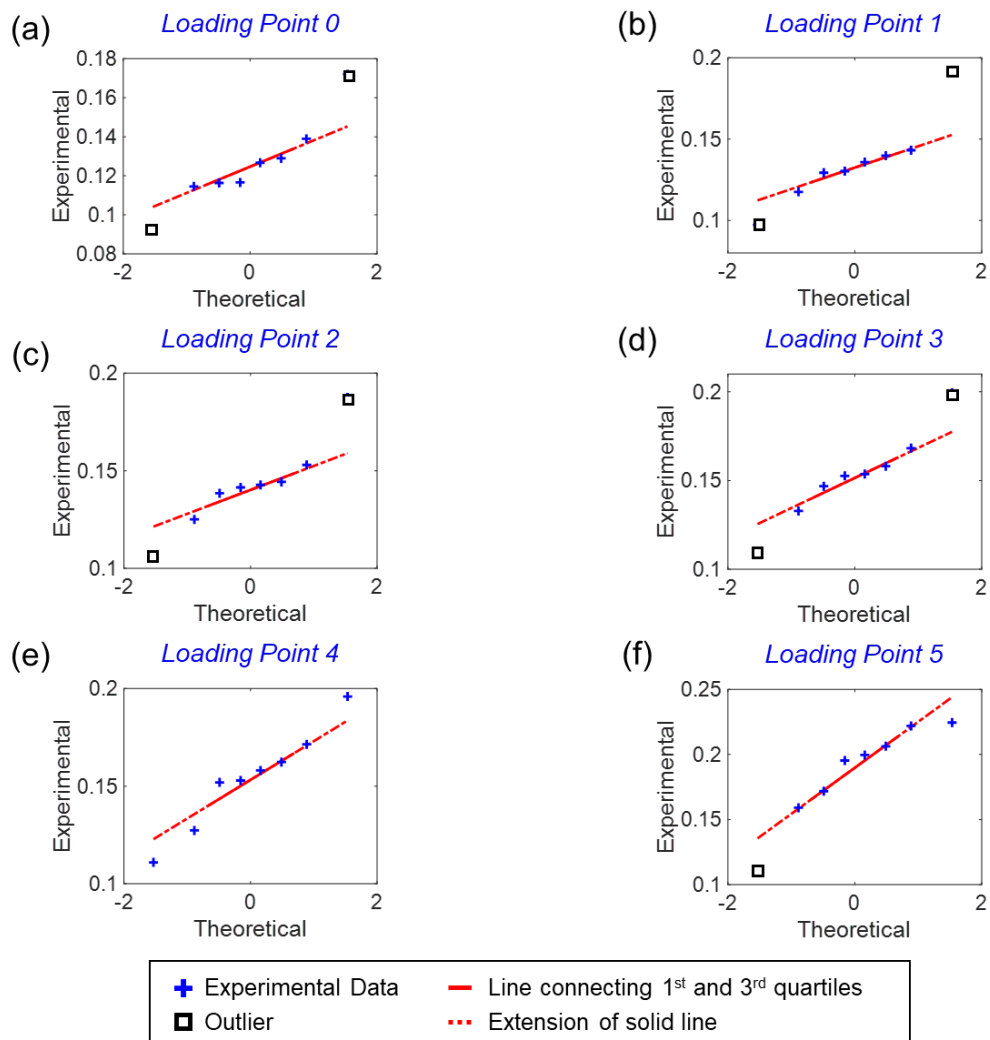
Figure S6 – Quantile-Quantile (QQ) plot for the quantified degree of optical anisotropy (DOA) – TVAL strut CT-leaflet insertions, considering various loading conditions: (a)-(f) Loading Points 0-5.
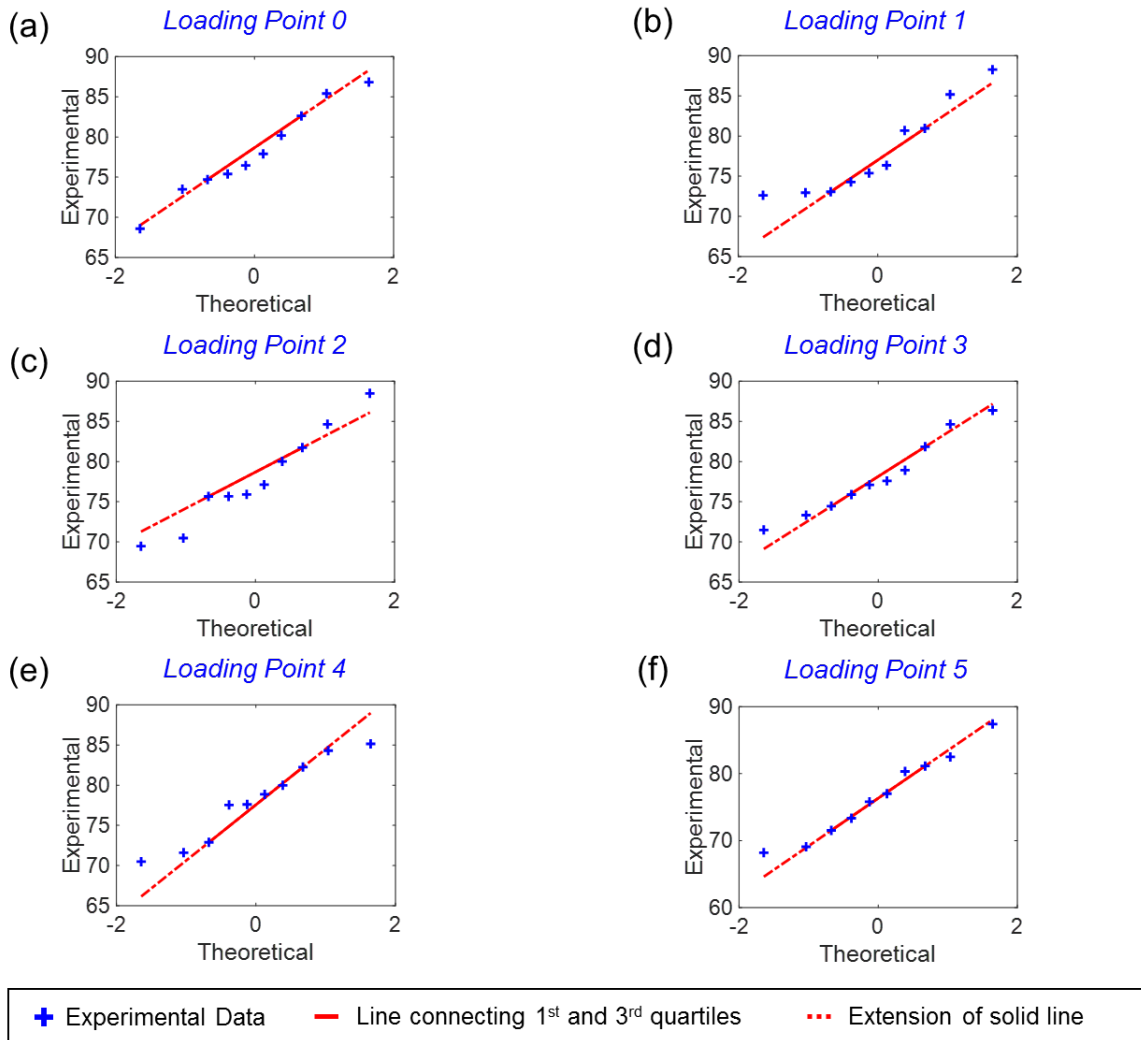
Figure S7 – Quantile-Quantile (QQ) plot for the predicted θ_{fiber} – MVAL strut CT-leaflet insertions, considering various loading conditions: (a)-(f) Loading Points 0-5.
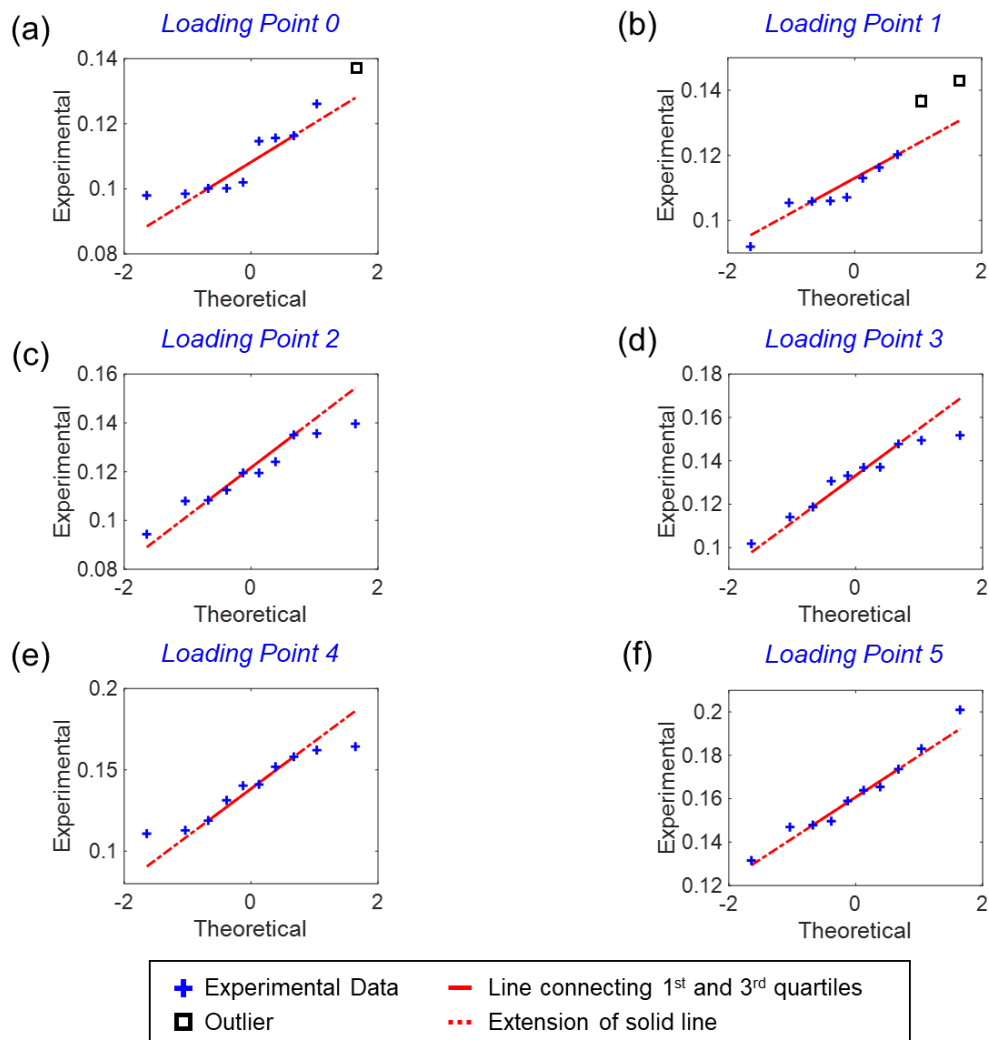
Figure S8 – Quantile-Quantile (QQ) plot for the quantified degree of optical anisotropy (DOA) – MVAL strut CT-leaflet insertions, considering various loading conditions: (a)-(f) Loading Points 0-5.